

ALMA Band 7 Observations of Water Lines in the Protoplanetary Disk of V883 Ori

HIROTO NAKASONE ,¹ SHOTA NOTSU ,^{2,3} TOMOHIRO C. YOSHIDA ,^{4,5} HIDEKO NOMURA ,^{4,5} TAKASHI TSUKAGOSHI ,⁶ TOMOYA HIROTA ,^{7,5} MITSUHIKO HONDA ,⁸ EIJI AKIYAMA ,⁹ ALICE S. BOOTH ,¹⁰ JEONG-EUN LEE ,^{11,12} AND SEOKHO LEE ,¹³

¹Department of Astronomy, Graduate School of Science, Kyoto University, Kitashirakawa-Oiwake-cho, Sakyo-ku, Kyoto 606-8502, Japan

²Department of Earth and Planetary Science, Graduate School of Science, The University of Tokyo, 7-3-1 Hongo, Bunkyo-ku, Tokyo 113-0033, Japan

³Star and Planet Formation Laboratory, Pioneering Research Institute, RIKEN, 2-1 Hirosawa, Wako, Saitama 351-0198, Japan

⁴National Astronomical Observatory of Japan, 2-21-1 Osawa, Mitaka, Tokyo 181-8588, Japan

⁵Department of Astronomical Science, The Graduate University for Advanced Studies, SOKENDAI, 2-21-1 Osawa, Mitaka, Tokyo 181-8588, Japan

⁶Faculty of Engineering, Ashikaga University, Ohmae-cho 268-1, Ashikaga, Tochigi, 326-8558, Japan

⁷Mizusawa VLBI Observatory, National Astronomical Observatory of Japan, 2-12 Hoshiga-oka, Mizusawa, Oshu-shi, Iwate 023-0861, Japan

⁸Faculty of Biosphere-Geosphere Science, Okayama University of Science, 1-1 Ridai-chou, Okayama 700-0005, Japan

⁹Division of Fundamental Education and Liberal Arts, Department of Engineering, Niigata Institute of Technology 1719 Fujihashi, Kashiwazaki, Niigata 945-1195, Japan

¹⁰Center for Astrophysics, / Harvard & Smithsonian, 60 Garden St., Cambridge, MA 02138, USA

¹¹Department of Physics and Astronomy, Seoul National University, 1 Gwanak-ro, Gwanak-gu, Seoul 08826, Republic of Korea

¹²SNU Astronomy Research Center, Seoul National University, 1 Gwanak-ro, Gwanak-gu, Seoul 08826, Republic of Korea

¹³Korea Astronomy and Space Science Institute, 776 Daedeok-daero, Yuseong, Daejeon 34055, Republic of Korea

ABSTRACT

The FU Orionis star V883 Ori provides a unique opportunity to probe the water snowline in a protoplanetary disk. During an accretion burst, the enhanced stellar luminosity heats the disk, sublimating ices and bringing volatile species into the gas-phase. The water snowline, located at ~ 80 au in the midplane, represents a key boundary for dust growth and volatile delivery to forming planets. We present Atacama Large Millimeter/submillimeter Array Band 7 observations of V883 Ori that detect two targeted water isotopologue transitions: para-H₂¹⁸O 5_{1,5}–4_{2,2} at 322 GHz and HDO 3_{3,1}–4_{2,2} at 335 GHz. After correcting for Keplerian rotation, we detect HDO and H₂¹⁸O at 23.6σ and 9.3σ , respectively. Rotational-diagram analysis using a Markov Chain Monte Carlo approach yields $T_{\text{rot}} = 116.89 \pm 12.81$ K and $N = (4.90 \pm 1.69) \times 10^{15} \text{ cm}^{-2}$ for H₂¹⁸O, and $T_{\text{rot}} = 87.46 \pm 4.95$ K and $N = (4.47 \pm 0.62) \times 10^{15} \text{ cm}^{-2}$ for HDO. These results imply water vapor abundances of $N_{\text{H}_2\text{O}}/N_{\text{H}_2} \sim 3 \times 10^{-7}$ – 5×10^{-6} and an HDO/H₂O ratio of $(0.4\text{--}2.0) \times 10^{-3}$ just inside the water snowline, broadly consistent with inheritance from protostellar envelopes. The HDO line in Band 7 is significantly weaker than predicted from Band 6 extrapolation, showing only $\sim 26\%$ of the expected strength. This attenuation can be explained by a more compact, hotter emitting region with an effective radius of ~ 53 au and/or frequency-dependent dust absorption that enlarges the apparent inner cavity at higher frequency. Our results highlight both the diagnostic power of water isotopologue lines and the need for higher angular resolution observations to resolve the water snowline and test these scenarios.

Keywords: Astrochemistry (75) — Protoplanetary disks (1300)

1. INTRODUCTION

Email: nakasone@kusastro.kyoto-u.ac.jp

Locating the position of the water snowline, which corresponds to the sublimation front of water molecules (e.g., C. Hayashi 1981; C. Hayashi et al. 1985), is cru-

cial for understanding the evolution of dust grains and the architecture of planetary systems (e.g., K. I. Öberg et al. 2011; A. Oka et al. 2011; S. Okuzumi et al. 2012; S. Okuzumi & R. Tazaki 2019; K. Ros & A. Johansen 2013; A. Banzatti et al. 2015; A.-M. A. Piso et al. 2015, 2016; L. A. Cieza et al. 2016; P. Pinilla et al. 2017; D. Schoonenberg & C. W. Ormel 2017; S. Mori et al. 2021; S. Notsu et al. 2022; K. Kondo et al. 2023). In addition, the location of the water snowline has implications for the delivery of water to terrestrial planets, offering clues to the origin of Earth’s oceans (e.g., A. Morbidelli et al. 2000, 2012, 2016; K. J. Walsh et al. 2011; S. Ida & T. Guillot 2016; S. Ida et al. 2019; T. Sato et al. 2016; S. N. Raymond & A. Izidoro 2017; T. Lichtenberg et al. 2021; A. Banzatti et al. 2023).

The H₂O snowline position depends on the mass accretion rate and luminosity of the central star, and on over the disk lifetime it moves inward as the disk evolves (e.g., A. Oka et al. 2011; D. Harsono et al. 2015; J. M. Miley et al. 2021; N. M. Murillo et al. 2022; F. Alarcón et al. 2024). Recently, water vapor emission from the inner warm disk and envelopes (> 100 K) of low-mass Class 0–I protostars has been investigated using such as NOEMA (NOrthern Extended Millimeter Array), ALMA (Atacama Large Millimeter/submillimeter Array), *Herschel* Space Observatory, and James Webb Space Telescope (JWST) (e.g., M. V. Persson et al. 2014; P. Bjerkeli et al. 2016; S. S. Jensen et al. 2019, 2021; D. Harsono et al. 2020; E. F. van Dishoeck et al. 2021, 2025; J. J. Tobin et al. 2023; S. Facchini et al. 2024; M. Leemker et al. 2025a), and HDO emission has also been detected toward the FU Ori object V1057 Cyg (J. K. Calahan et al. 2024). The water vapor abundances and the degree of deuteration of water in the warm region of low-mass Class 0 protostars are also reported, and the HDO/H₂O ratios are found to lie roughly between (6 × 10⁻⁴) and (2 × 10⁻³) (e.g., M. V. Persson et al. 2014; S. S. Jensen et al. 2019, 2021; D. Harsono et al. 2020; S. Notsu et al. 2021; E. F. van Dishoeck et al. 2025).

V883 Ori is classified as an FU Orionis (FUor) object located in the Orion A L1641 molecular cloud. It is currently in a transitional phase between Class I and Class II, characterized by a thin envelope and a massive circumstellar disk (F. Alarcón & E. A. Bergin 2024). The source is undergoing a rapid luminosity increase attributed to an accretion burst onto the central protostar. The mass of the central star has been estimated at approximately 1.3 M_⊙, surrounded by a well-developed Keplerian rotating disk with a mass of at least 0.3 M_⊕ and situated at a distance of 400 pc (M. Kounkel et al. 2018). Its bolometric luminosity is about 200 L_⊙ (T. P. Greene et al. 2008; L. A. Cieza et al. 2016; E. Furlan

et al. 2016; J.-E. Lee et al. 2019; D. A. Ruíz-Rodríguez et al. 2022).

The elevated luminosity of the central protostar increases the disk temperature, which leads to the thermal desorption of molecules previously frozen onto dust grain surfaces, enabling their detection in the gas phase (M. L. R. van ’t Hoff et al. 2018; J.-E. Lee et al. 2019; J. J. Tobin et al. 2023; Y. Yamato et al. 2024; M. Leemker et al. 2025b). Moreover, since the duration of the accretion outburst (~100 years) is much shorter than the timescales required for significant chemical processing in the gas-phase (e.g., H. Nomura et al. 2009), observations can capture these freshly sublimated molecules from dust grain surfaces before they undergo significant chemical alteration in the gas-phase. This allows near-direct probing of the disk ice composition. Based on the intensity break observed in the 0.1 mm continuum emission, L. A. Cieza et al. (2016) inferred that the water snowline at the disk midplane lies within approximately 42 au of the central star. On the disk surface, the water snowline (water snow-surface) may extend out to around 160 au (M. L. R. van ’t Hoff et al. 2018; J.-E. Lee et al. 2019; M. Leemker et al. 2021). However, more recent ALMA observations of HDO by J. J. Tobin et al. (2023) indicate that the water snowline at the midplane is located at a radius of about 80 au.

In addition to water, the detection of complex organic molecules (COMs), whose snowline positions are close to water, represents a key observational challenge in studies of disks. COMs are of particular interest because they are considered potential precursors of prebiotic species that may have contributed to the origin of life on Earth (C. Ceccarelli et al. 2023). Using ALMA Band 7 observations, M. L. R. van ’t Hoff et al. (2018) reported the first detection of CH₃OH emission in the V883 Ori disk. Subsequent studies have identified multiple lines of COMs, including isotopologues, toward this source (J.-E. Lee et al. 2019; Y. Yamato et al. 2024; J.-H. Jeong et al. 2025; A. M. A. Fadul et al. 2025b,a; S. Zeng et al. 2025). They found that the COMs abundance ratios with respect to methanol are significantly higher than those in the warm protostellar envelopes of IRAS 16293-2422 and similar to the ratios in the solar system comet 67P/Churyumov-Gerasimenko, suggesting the efficient (re)formation of COMs in protoplanetary disks. In addition, Y. Yamato et al. (2024) also constrained the ¹²C/¹³C and D/H ratios of COMs in protoplanetary disks for the first time (see also J.-H. Jeong et al. 2025; A. M. A. Fadul et al. 2025b; S. Zeng et al. 2025). The D/H ratios of methyl formate are slightly lower than the values in IRAS 16293-2422, possibly pointing to the destruction and reformation of COMs in the disk (Y.

Yamato et al. 2024). As demonstrated by J. J. Tobin et al. (2023), identifying and characterizing water isotopologue emission—particularly determining their intensities and emitting regions—requires careful treatment of potential line blending with nearby contaminated lines, which presents a significant challenge both observationally and in the subsequent analysis.

In this paper, we present new observations of water isotopologue lines toward the V883 Ori disk conducted with ALMA Band 7. Previous studies have reported detections of H_2^{18}O at 203 GHz in Band 5 and HDO lines at 225 and 241 GHz in Band 6 (J. J. Tobin et al. 2023) and a marginal detection of the HDO 335 GHz line in Band 7 was reported by J.-E. Lee et al. (2019). Furthermore, the detection of D_2O at 316 GHz in Band 7 has also been reported (M. Leemker et al. 2025b). Following up on these works and motivated by the theoretical discussions (S. Notsu et al. 2016, 2017, 2018) and previous observational attempts (S. Notsu et al. 2019; A. D. Bosman & E. A. Bergin 2021; S. Facchini et al. 2024), we report ALMA Band 7 observations aimed at detecting three water transitions— H_2^{16}O at 321 GHz, H_2^{18}O at 322 GHz, and HDO at 335 GHz. Although the H_2^{16}O line was not detected, we successfully detected the H_2^{18}O and HDO lines in the V883 Ori disk. We describe the observational and imaging procedures in Section 2, present a detailed analysis of the disk-integrated spectra including these detections in Section 3, and discuss the implications for the physical and chemical structure of the V883 Ori disk as well as the isotopic chemistry of water in protoplanetary disks in Section 4. A summary of our results is provided in Section 5.

2. OBSERVATIONS

2.1. ALMA Band 7 Observations

V883 Ori was observed in Band 7 with the ALMA program 2021.1.00115.S (Principal Investigator: S. Notsu), targeting the ortho- H_2^{16}O 321.23 GHz line, the para- H_2^{18}O 322.47 GHz line, and the HDO 335.40 GHz line. The molecular coefficients for the three transitions are reported in Table 1 (see also S. Notsu et al. 2018, 2019). We observed the target source on September 7, 2022, using 43 ALMA antennas, in one execution block. The on-source integration time was 42 minutes, under atmospheric conditions with a precipitable water vapor (PWV) of 0.3 mm. The baseline lengths ranged from 15.1 m to 783.5 m, yielding an angular resolution of $0''.3$ and a maximum recoverable scale (MRS) of $4''.2$. The MRS is sufficient to recover the V883 Ori disk, whose dust and gas (C^{18}O) emission extend to ~ 125 au ($\sim 0''.3$) and ~ 320 au ($\sim 0''.8$), respectively (L. A. Cieza et al. 2016). For calibration, we used J0423–0120 as the band-

Table 1. Parameters of Our Target Water Lines

Isotope	$J_{K_a K_c}$	Frequency (GHz)	A_{ul} (s^{-1})	E_u (K)
o- H_2^{16}O	$10_{29} - 9_{36}$	321.22568	6.17×10^{-6}	1862.2
p- H_2^{18}O	$5_{15} - 4_{22}$	322.46517	1.06×10^{-5}	467.9
HDO	$3_{31} - 4_{22}$	335.39550	2.61×10^{-5}	335.3

pass and amplitude calibrator, and J0607–0834 as the phase calibrator. Each isotope was observed with an appropriate correlator setup, and the detailed properties of the spectral windows (SPWs) corresponding to each isotope are summarized in Table 2.

2.2. Calibration and Imaging

Initial calibrations were performed by the ALMA staff using the standard ALMA calibration pipeline version 2022.2.0.64. Subsequent self-calibration and imaging were performed using the Common Astronomy Software Applications (CASA; CASA Team et al. (2022)) version 6.5.3.28. Before making the line images, we first made the image of the continuum emission using the spw tuned for detecting the continuum emission, in order to perform a hybrid-mapping with self-calibration. The pipeline-calibrated data were first imaged with the CLEAN algorithm using the CASA task `tclean`. The robust weighting was used for the imaging with a robustness parameter of 0.5. We employed the multiscale clean with scales corresponding to 0, 1, 3, 5, and 10 times of the synthesized beam. After the initial clean image of the continuum emission was created, we performed some rounds of self-calibration and CLEAN imaging (i.e., a hybrid-mapping) for the continuum visibilities using the CASA tasks `gaincal`, `applycal`, and `tclean`. We conducted 3 rounds of phase-only self-calibration by changing solution intervals from 300 to 6 sec, followed by 1 round of amplitude self-calibration. The final CLEAN image was thus improved by a factor of 10 with respect to the initial one. The synthesized beam of the final continuum map was $0''.39 \times 0''.30$ with a position angle of -78.3° , and the rms noise level of the map was 0.28 mJy beam $^{-1}$.

By using the calibration table obtained with the self-calibration above, we created the CLEAN images of the target lines. After applying the calibration table to the visibilities of the target lines with `applycal`, we performed the continuum subtraction with the task `uvcontsub` to the calibrated visibilities of each line. The ranges of the `fitspws` parameter were set to (0–200, 1600–

Table 2. Properties of Image Cubes

Isotope	Bandwidth	Channel Width	Vel. Res.	Beam Size (P.A.)	rms
	(MHz)	(MHz)	(km s^{-1})	(km s^{-1})	(mJy beam^{-1})
$\text{o-H}_2^{16}\text{O}$	234	0.122	0.114	0.132	$0.^{\prime\prime}41 \times 0.^{\prime\prime}29$ (-75°)
$\text{p-H}_2^{18}\text{O}$	234	0.244	0.227	0.262	$0.^{\prime\prime}40 \times 0.^{\prime\prime}31$ (-75°)
HDO	117	0.122	0.109	0.126	$0.^{\prime\prime}39 \times 0.^{\prime\prime}28$ (-75°)

1919), (0–140, 880–959), and (0–130, 240–330, 610–700) channels for ortho- H_2^{16}O , para- H_2^{18}O , and HDO, respectively. The line images were created using CLEAN from the continuum-subtracted visibilities. We adopted the briggs weighting with a robust parameter of 0.5. The multiscale CLEAN was employed with scale parameters corresponding to 0, 1, 3, 5, and 10 times of the synthesized beam of each line map. The synthesized beamsize and the rms noise level of the CLEAN maps were summarized in Table 2.

3. DATA ANALYSIS AND RESULT

3.1. Spectrum Extraction

The resulting data cubes were used to generate spectra by integrating over an aperture with a radius of $0.^{\prime\prime}4$. Figures 1, 2, and 3 show the spectra obtained for detecting the H_2^{16}O , H_2^{18}O , and HDO lines, respectively. In the top panels of Figures 1, 2, and 3, double-peaked line profiles are visible, reflecting the Keplerian rotation of the disk.

Next, to increase the sensitivity of the line detection and to resolve blended lines, we applied a correction for Keplerian rotation. The correction assumes that the disk gas is in Keplerian rotation and removes the Doppler shifts associated with this orbital motion. The spectra were extracted from a radius of $0.^{\prime\prime}4$ using the `integrated_spectrum()` function from the GoFish Python package (R. Teague 2019), which deprojects the disk and shifts each line to the systemic velocity (4.25 km s^{-1}), producing single-peaked profiles and allowing for easier identification by reducing blended components. To correct for Keplerian rotation, the stellar mass, distance, inclination and position angle ($1.29 M_{\odot}$, 400 pc, 38.3° and 32° respectively) are provided as input parameters to the `integrated_spectrum()` function. These values allow the function to deproject the disk and apply velocity alignment and line broadening correction accordingly. In the `integrated_spectrum()` function, an inclination of 38.3° and a position angle of 32° are assumed, based on previous studies (L. A. Cieza et al. 2016; J. J. Tobin et al. 2023). We further assume that the emission arises from the disk midplane and ne-

glect any vertical structure. The resulting spectra are shown in the bottom panels of Figures 1, 2, and 3. After the correction for Keplerian rotation, each line exhibits a single-peaked profile, demonstrating that the Doppler shifts associated with the disk’s orbital motion have been properly removed.

The observed spectra and those corrected for Keplerian rotation, without the overlaid model components, are presented separately in Appendix Figures 11 and 12.

3.2. Spectral Fitting and Line Identification

In these single-peaked spectra, obtained by correcting for Keplerian rotation, we attributed spectral features to nearby contaminated lines if they exhibited peaks exceeding a 5σ significance threshold and corresponded to transitions that had not yet been assigned. To remove contamination from water lines caused by nearby contaminated lines, we constructed template spectra that could be applied to each detected line.

Specifically, to model the emission features of HDO, H_2^{18}O , and nearby contaminated lines, which could be COMs lines, we created a template spectrum using an isolated CH_3CHO $\text{vt}=0$ $18_{0,18}-17_{0,17}$, E 335.3825 GHz line. This line had been previously identified and assigned in the same spectral window by J.-E. Lee et al. (2019) as part of their line survey.

After subtracting the baseline to remove any remaining slope, the spectrum was scaled so that its peak intensity equals 1.0. To generate a symmetric template, the spectrum was mirrored about its center of the line and averaged with the original profile, producing an idealized spectral shape suitable for modeling. We constructed template spectra using both the double-peaked profile obtained before correcting for Keplerian rotation and the single-peaked profile obtained after the correction.

To accurately identify the water isotopologue lines, it was necessary to first remove the contribution from nearby contaminated lines that blend with them. To this end, we began by determining the central frequencies of the blended lines using the Keplerian-corrected spectra, which provide deblended, single-peaked profiles suitable for line identification. In Figures 1, 2 and 3, these $> 5\sigma$

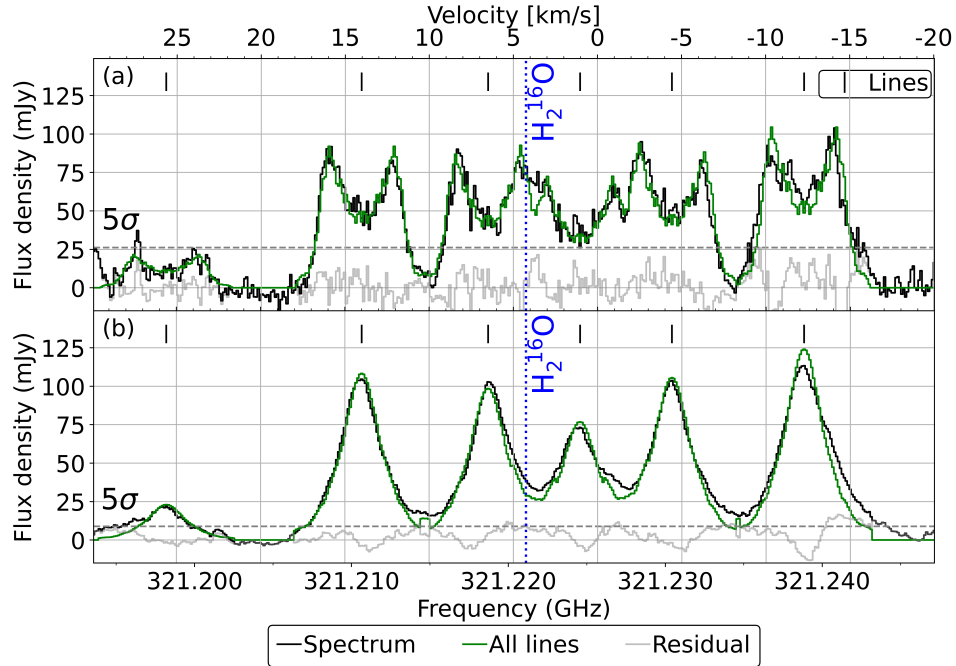


Figure 1. (a) Observed spectrum around the H_2^{16}O 321 GHz line (black solid line). (b) Spectrum after correction for Keplerian rotation (black solid line). In both (a) and (b), the systemic velocity has not been corrected; the blue dotted lines indicate the source velocity of V883 Ori (4.25 km s^{-1}) and mark the expected frequency of the H_2^{16}O transition. The green solid lines represent the combined fitting models of the nearby contaminated lines. The gray solid lines show the residuals obtained by subtracting the model spectra from the observed and Keplerian-corrected spectrum. The vertical black ticks indicate the central frequencies of the nearby contaminated lines (see Line 1-6 in Table 3). The gray dashed lines indicate the 5σ noise level, derived from the standard deviation of spectra taken in an off-source region; (a) from the raw spectrum, and (b) from the Keplerian-rotation-corrected spectrum.

peaks are marked by short black ticks above the spectra, and were treated as nearby contaminated lines. A list of these nearby contaminated lines, together with their rest frequencies, is provided in Table 3. Among the lines in Table 3, those in SPW 1 have central frequencies consistent with the transitions of $^{13}\text{CH}_3\text{OH}$ and CH_3OCHO detected in Orion KL with ALMA Band 7 observations by [T. Hirota et al. \(2014\)](#) (see their Fig. 8), suggesting that these identifications are plausible.

The spectral modeling was performed by fitting the observed spectra as a linear combination of the scaled template profiles. Using the identified frequencies of each component as the above method, we employed the `scipy.optimize.minimize` function to determine the best-fitting multiplicative scaling factors. The results of this fitting procedure are presented in Figures 1, 2 and 3. In these figures, the green curves represent the best-fit models including both nearby contaminated lines and water emission components, while the blue curves isolate the contribution from the water lines alone. Using this approach, HDO was detected at 6.7σ and 23.6σ before and after correction for Keplerian rotation, respectively. H_2^{18}O was tentatively detected at 3.1σ before the correction, and successfully detected at 9.3σ after

the correction. In contrast, H_2^{16}O was not detected. Although it should be more abundant than the other two isotopologues, its 321 GHz transition has a much higher upper state energy than those in other two observed H_2^{18}O and HDO transitions (see Table 1); as a result, its emission is likely buried beneath the upper limits of other adjacent transition lines.

Following the spectral fitting, we derived the integrated intensities of the HDO and H_2^{18}O lines by integrating the model spectra corresponding to the water line components. Specifically, the integration was performed over the blue curves shown in Figures 2 and 3. For the o- H_2^{16}O 321 GHz line, which was not detected in this study, we estimated the integrated intensity that the modeled double-peaked spectrum would yield if its peaks reached the 3σ level, and adopted this value as the upper limit. The results are summarized in Table 4.

We note that our approach differs from that of [J. J. Tobin et al. \(2023\)](#), who used the isolated CH_3OH 242 GHz lines detected in Band 6 to construct a template spectrum, and derived the integrated intensity by subtracting the modeled COM emission from the observed spectrum and integrating the residuals. We performed the fitting using template spectra from both CH_3CHO

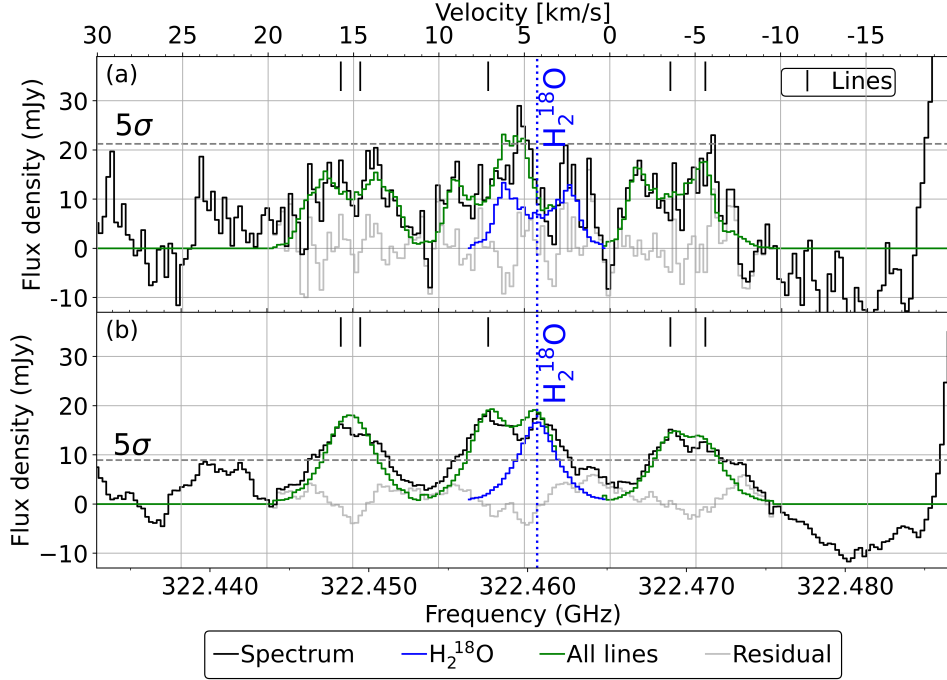


Figure 2. Similar to Figure 1, but for the H_2^{18}O 322 GHz line. The blue solid lines show the fitted models for the H_2^{18}O line. The green solid lines represent the combined fitting models of the H_2^{18}O line and the nearby contaminated lines. The vertical black ticks indicate the central frequencies of the nearby contaminated lines (see Line 7–11 in Table 3).

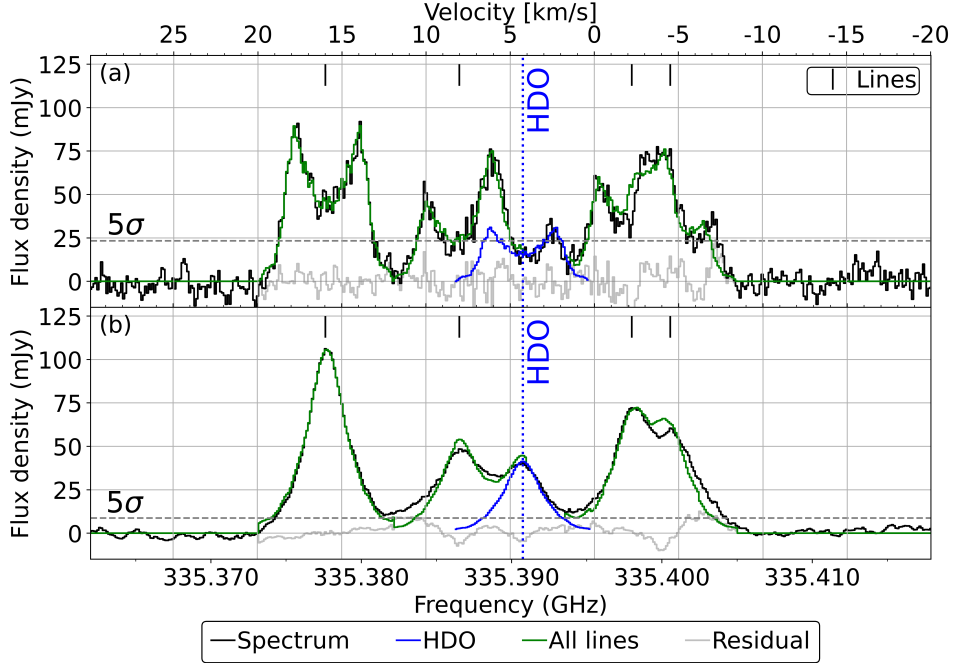


Figure 3. Similar to Figure 2, but for the HDO 335 GHz line. The vertical black ticks indicate the central frequencies of the nearby contaminated lines (see Line 12–14 in Table 3).

335 GHz and CH_3OH 242 GHz. Nevertheless, the integrated intensities of the fitted water model spectra are consistent within 1σ uncertainties (see Appendix B).

3.3. Spatial Distributions

3.3.1. Channel Maps

Figures 4 and 5 present the channel maps of the HDO and H_2^{18}O emission, overlaid with the corresponding

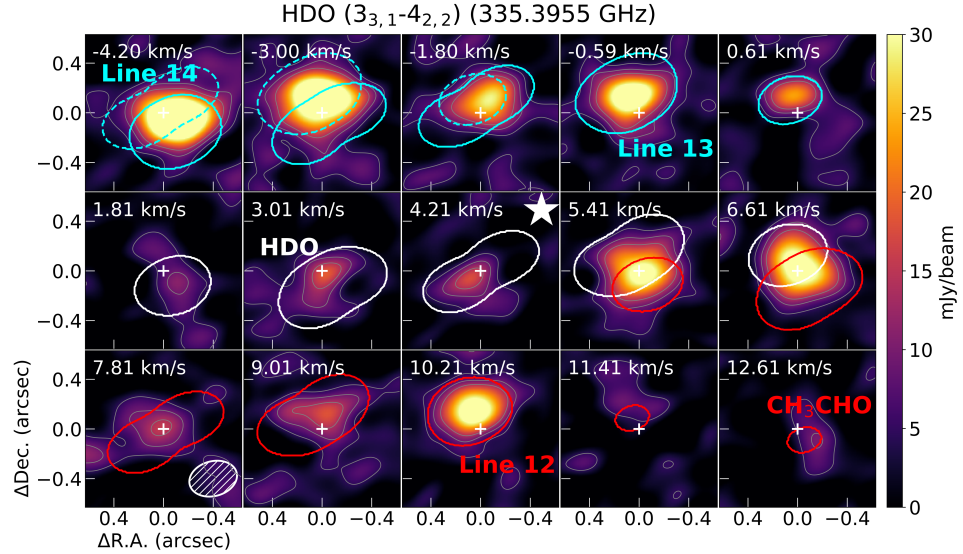


Figure 4. Channel maps around the frequency of the HDO line at 335 GHz. The position of the protostar is marked with a white cross, and the channels closest to the systemic velocity of V883 Ori (4.25 km s^{-1}) are indicated by a star in the upper right corner. Thin gray contours represent 1, 2, and 3σ levels. To clearly highlight the emission region of the HDO line, the emission is saturated in some panels. The synthesized beam is shown in the lower right corner of the bottom-left panel. The Keplerian mask for the HDO emission is drawn as a thick white line, and the masks corresponding to the blended nearby contaminated lines and COM line; two in blueshifted region and two in redshifted region of the HDO line are shown as thick cyan and red lines, respectively.

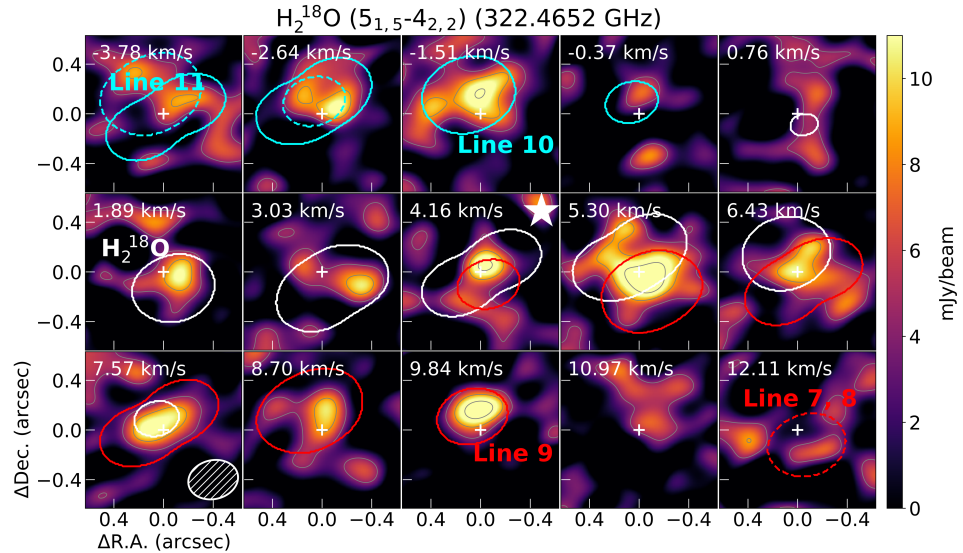


Figure 5. Similar to Figure 5, but for the H_2^{18}O line at 322 GHz. The Keplerian mask for the H_2^{18}O emission is drawn as a thick white line, and the masks corresponding to the nearby contaminated lines; two in blueshifted region and three in redshifted region of the H_2^{18}O are shown as thick cyan and red lines, respectively.

Keplerian masks generated with the `keplerian_mask` code (R. Teague 2020). Keplerian masks for the contaminating lines are also shown to indicate the expected velocity ranges and spatial locations of overlapping emission. The parameters used to construct these masks are listed in Table 3, and were applied consistently across both the water isotopologue lines and the nearby con-

taminated lines. As evident in the spectra presented in Figures 1, 2, and 3, the target water lines exhibit partial blending with nearby contaminated lines, which is also apparent in the channel maps. However, for both HDO and H_2^{18}O , minimal contamination is seen within the velocity range $1.45\text{--}3.45 \text{ km s}^{-1}$. Within this range, the emission is expected to originate predominantly from

Table 3. Keplerian mask parameters for water isotopologues and contaminated lines blended with water

Line	Rest freq. (GHz)
SPW 1	
Line 1	321.2028
Line 2	321.2152
Line 3	321.2233
(H ₂ ¹⁶ O 10 _{2,9} -9 _{3,6}) ^a	(321.2257)
Line 4	321.2291
Line 5	321.2350
Line 6	321.2434
SPW 2	
Line 7	322.4528
Line 8	322.4540
Line 9	322.4621
H ₂ ¹⁸ O 5 _{1,5} -4 _{2,2}	322.4652
Line 10	322.4736
Line 11	322.4758
SPW 3	
CH ₃ CHO vt=0, 18 _{0,18} -17 _{0,17} , E	335.3825
Line 12	335.3913
HDO 3 _{3,1} -4 _{2,2}	335.3955
Line 13	335.4028
Line 14	335.4053

^aH₂¹⁶O was not detected.

NOTE— SPWs 1, 2, and 3 correspond to the spectral windows targeting the H₂¹⁶O 321 GHz, H₂¹⁸O 322 GHz, and HDO 335 GHz lines, respectively. For all lines, the Keplerian mask was generated using the `keplerian_mask` code (R. Teague 2020), adopting the following parameters: Smoothing = 0.65, R_{max} = 0''.3, R_{min} = 0''.1, Z/R = 0.4, and ΔV = 0.1 km s⁻¹. Line 1-14 denotes an unidentified spectral feature associated with a 5 σ peak in the stacked spectrum.

the water lines, allowing for a robust extraction of uncontaminated water emission.

3.3.2. Moment 0 Extraction

Figures 6 and 7 show the velocity-integrated intensity maps (moment 0 maps) of the selected water isotopologue transitions. In each figure, the left panel presents the moment 0 map generated using the Keplerian mask defined by the parameters listed in Table 3 for the target

Table 4. Integrated intensity, T_{rot} , and N_{thin}

Isotope	I_{int} (mJy km s ⁻¹)	T_{rot} (K)	$\log_{10}(N_{\text{thin}})$ (cm ⁻²)
(o-H ₂ ¹⁶ O) ^a	≤ 60.89		
p-H ₂ ¹⁸ O	52.06 ± 7.48		
	Median: 119.33 ^{+15.57} _{-11.98}	119.33 ^{+15.57} _{-11.98}	15.68 ^{+0.09} _{-0.09}
	MAP: 116.89 ± 12.81	116.89 ± 12.81	15.69 ± 0.15
HDO	123.73 ± 6.15		
	Median: 87.93 ^{+5.23} _{-4.78}	87.93 ^{+5.23} _{-4.78}	15.65 ^{+0.03} _{-0.03}
	MAP: 87.46 ± 4.95	87.46 ± 4.95	15.65 ± 0.06

^a3 σ upper limits are estimated for non-detection.

water line. The right panel shows the moment 0 map integrated over a velocity range (1.45–3.45 km s⁻¹) identified from the channel maps as being minimally contaminated by other lines; no masking was applied except for this velocity selection. The spatial distribution of the water line emission indicates that it originates from within the disk region (approximately 0''.3 or \sim 120 au in radius). However, the emission is only marginally spatially resolved at the current resolution of \sim 0''.3–0''.4, and the central cavities reported in the Band 5 and Band 7 data by J. J. Tobin et al. (2023) are not detected due to the limitation of the lower spatial resolution.

3.4. Rotation Temperature and Column Density

In Figures 8 and 9, we constructed rotational diagrams for HDO and H₂¹⁸O by combining our new ALMA Band 7 observations of the HDO 335 GHz and H₂¹⁸O 322 GHz lines with the HDO 225 and 241 GHz transitions in Band 6 and the H₂¹⁸O 203 GHz line in Band 5 reported by J. J. Tobin et al. (2023).

We adopted the assumptions of optically thin emission and a uniform excitation temperature across the relevant energy range. Our methodology follows that of S. Facchini et al. (2024).

Partition functions as a function of temperature were taken from the JPL database (H. M. Pickett et al. 1998) for HDO and H₂¹⁸O, interpolating between tabulated values when necessary. We employed the full partition function, which assumes an ortho-to-para ratio of 3:1 for H₂¹⁸O, and therefore did not rescale individual ortho and para line fluxes.

We performed a linear regression in the $\log(N/g_u)$ versus E_u space using the `emcee` sampler to derive the rotational temperature T_{rot} and the column density N . In this analysis, the column density in each energy level N_u

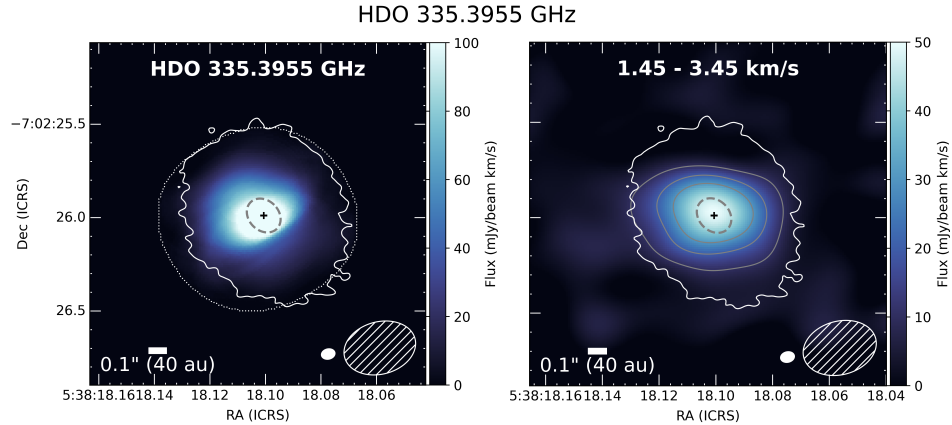


Figure 6. The HDO 335 GHz integrated intensity map created using a Keplerian mask (the left panel) and that integrated over the velocity range 1.45–3.45 km s^{−1} (the right panel). The contours in the right panel represent intensity levels at 5 σ , 10 σ and 15 σ , where 1 σ corresponds to 2.01 mJy beam^{−1} km s^{−1}, computed by integrating over 1.45–3.45 km s^{−1}. The 1.45–3.45 km s^{−1} velocity range was selected to minimize contamination from other lines. The position of the protostar is marked with a black cross. The optically thick region suggested by previous studies is indicated by the thick gray line at the center of each panel. The hatched ellipses in the lower right corners denote the synthesized beam size of the line observation ($\sim 0''.28 \times 0''.39$) The solid white line outlines the emission region of the dust continuum, while the filled white ellipse indicates the synthesized beam of the dust continuum observation ($\sim 0''.08$). In the left panel, the dotted white line marks the outer extent of the Keplerian mask.

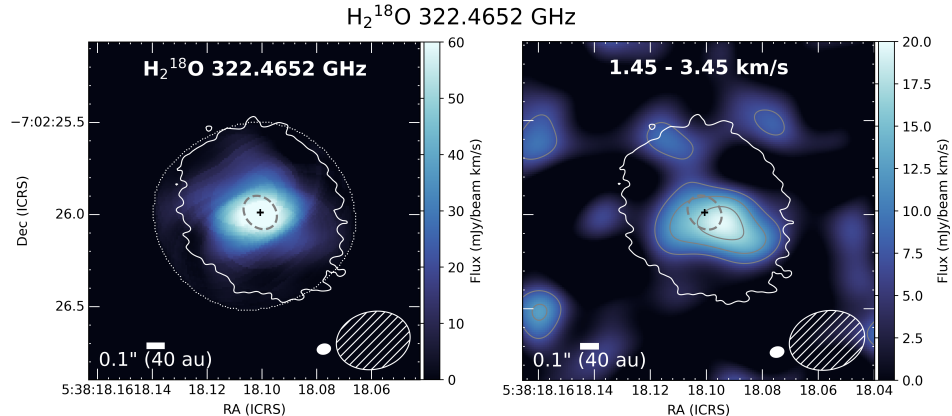


Figure 7. Similar to Figure 6, but for H₂¹⁸O 322 GHz line. The contours in the right panel represent intensity levels at 3 σ , 5 σ and 7 σ , where 1 σ corresponds to 2.39 mJy beam^{−1} km s^{−1}, computed by integrating over 1.45–3.45 km s^{−1}. The hatched ellipses in the lower right corners denote the synthesized beam size of the line observation ($\sim 0''.31 \times 0''.40$).

is related to the total column density N through

$$N = \frac{N_u}{g_u} Q_{\text{rot}}(T_{\text{ex}}) e^{\frac{E_u}{T_{\text{ex}}}} \quad (1)$$

where g_u is the statistical weight of the upper state, E_u is its energy, and $Q_{\text{rot}}(T_{\text{ex}})$ is the rotational partition function at the excitation temperature T_{ex} . By fitting a straight line to $\log(N_u/g_u)$ as a function of E_u , the slope yields $1/T_{\text{rot}}$, while the intercept provides N . This approach assumes local thermodynamic equilibrium (LTE) and that the lines are optically thin. The sampling employed 32 walkers, 5,000 steps, and a 3,000-step burn-in. Molecular coefficients were taken from Table 1. In the optically thin assumption, N_{thin} represents the column

density and T_{rot} the rotational temperature, where E_u is the upper state energy and g_u the upper state degeneracy. Each rotational diagram was fitted with best-fit parameters for N_{thin} and T_{rot} for HDO and H₂¹⁸O, respectively.

The marginalized posterior distributions obtained from the MCMC sampling are shown in Figures 8 and 9, with the corresponding corner plots displayed in the right panels of each figure. For each molecule, both the median values (with uncertainties corresponding to the 16th and 84th percentiles) and the maximum a posteriori (MAP) estimates are reported. The results of the MAP estimation indicate that H₂¹⁸O has a rota-

tional temperature of 116.89 ± 12.81 K and a logarithmic column density of $\log(N[\text{cm}^{-2}]) = 15.69 \pm 0.15$, whereas HDO shows a lower rotational temperature of 87.46 ± 4.95 K and a logarithmic column density of $\log(N[\text{cm}^{-2}]) = 15.65 \pm 0.06$. Based on these values, the optical depths of the lines are on the order of 2×10^{-2} , consistent with the assumption that they are optically thin. The derived excitation temperatures and column densities, along with the integrated line intensities, are summarized in Table 4. All uncertainties include the 10% absolute flux calibration uncertainty of ALMA.

In the rotational diagram for HDO, the 335 GHz line observed in ALMA Band 7 falls significantly below the linear trend defined by the two transitions detected in Band 6 (at 225 and 241 GHz). This deviation indicates that the Band 7 line is substantially weaker than expected based on the rotational temperature and column density derived from the Band 6 data. Quantitatively, the observed intensity of the Band 7 transition is only 26% of the value predicted by extrapolating the linear fit from the two Band 6 lines to the upper state energy of the 335 GHz transition. In other words, the line is roughly a quarter as strong as expected. As a result, including the Band 7 line in the fit yields a significantly lower rotational temperature of ~ 87.4 K, compared to 186.4 K derived from the Band 6 data alone (see Figure 14). For the rotational diagram constructed from the two H_2^{18}O lines observed in Bands 5 and 7, the derived excitation temperature is $T_{\text{ex}} = 119$ K, lower than the $T_{\text{ex}} = 203$ K inferred from the rotational diagram based on the two Band 6 HDO lines. This suggests that the intensity of the Band 7 H_2^{18}O line may also be weaker than expected from the observations in Bands 5 and 6. We interpret this discrepancy as a suppression of the Band 7 HDO line intensity in particular, and explore potential causes for this attenuation in Section 4.3.

3.5. Total Column Densities at Several Excitation Temperatures

Based on the H_2^{16}O , H_2^{18}O and HDO lines in Bands 5, 6, and 7, the total column densities were calculated under the assumption of several excitation temperatures (75, 180, and 225 K) in order to investigate the water abundance and the D/H ratio under different thermal conditions. The results are summarized in Table 5. The derived total column density is significantly higher compared to those derived from other detected water lines especially when we assume $T_{\text{ex}} = 75$ K. This is because the H_2^{16}O 321 GHz line has a much higher upper state energy compared to the other isotopic water lines (see Table 1).

Although the H_2^{18}O line intensities in Band 7 are weaker than those in Band 5 (see Table 9), the derived column density N is larger in Band 7 at $T_{\text{ex}} = 75$ K. This is because the upper state energy of the Band 5 H_2^{18}O line ($E_u(203 \text{ GHz}) = 203.7$ K) is much lower than that of the Band 7 H_2^{18}O line ($E_u(322 \text{ GHz}) = 467.9$ K). When Equation (1) is treated as a function of T_{ex} , the exponential term gives a much larger contribution in Band 7, resulting in a higher value of the total column density N . This trend is also observed in the comparison between the Band 6 and Band 7 HDO lines: the upper state energies of the Band 6 HDO lines are $E_u(225 \text{ GHz}) = 167.6$ K and $E_u(241 \text{ GHz}) = 95.2$ K, whereas the Band 7 HDO line has $E_u(335 \text{ GHz}) = 335.3$ K, which is sufficiently higher. As a result, the derived column density N at $T_{\text{ex}} = 75$ K is larger in Band 7.

Furthermore, for the Band 5 and Band 6 H_2^{18}O and HDO lines, the derived column density N is larger at $T_{\text{ex}} = 225$ K than at $T_{\text{ex}} = 180$ K. In contrast, for the Band 7 H_2^{18}O and HDO lines, N becomes smaller at $T_{\text{ex}} = 225$ K than at $T_{\text{ex}} = 180$ K. This behavior arises because the upper state energies E_u of the Band 7 lines are higher, and thus the decrease in the exponential term of Equation (1) has a stronger impact.

4. DISCUSSION

4.1. Water abundance

We assume the initial gas surface density profile to follow a tapered power-law distribution (D. Lynden-Bell & J. E. Pringle 1974; L. Hartmann et al. 1998; D. Harsono et al. 2020):

$$\Sigma_g(r) = \Sigma_c \left(\frac{r}{r_c} \right)^{-\gamma} \exp \left[- \left(\frac{r}{r_c} \right)^{2-\gamma} \right] \quad (2)$$

where $r_c = 75$ au (M. L. R. van 't Hoff et al. 2018; M. Leemker et al. 2021), $\gamma = 1.25$ (A. Houge et al. 2024), the disk mass is assumed to be $M_{\text{disc}} \approx 0.3M_{\odot}$ (L. A. Cieza et al. 2018; M. Leemker et al. 2021), and

$$\Sigma_c = \frac{M_{\text{disc}}(2-\gamma)}{2\pi r_c^2}. \quad (3)$$

This method to estimate the initial gas surface density profile is based on D. Harsono et al. (2020). Using the derived surface density profile, we calculate the H_2 column density as

$$N_{\text{H}_2} = \frac{\Sigma_g}{\mu_{\text{H}_2} m_{\text{H}}} \quad (4)$$

with $\mu_{\text{H}_2} = 2.8$ (J. Kauffmann et al. 2008). At $r = 80$ au, corresponding to the water snowline, we obtain $N_{\text{H}_2} = 3.9 \times 10^{24} \text{ cm}^{-2}$.

Table 5. Total column density N at different excitation temperatures T_{ex}

Band	Line	Total column density (cm^{-2})		
		$(T_{\text{ex}} = 75 \text{ K})$	$(T_{\text{ex}} = 180 \text{ K})$	$(T_{\text{ex}} = 225 \text{ K})$
Band 5	H_2^{18}O (203 GHz)	$(8.11 \pm 1.42) \times 10^{15}$	$(6.08 \pm 1.06) \times 10^{15}$	$(6.65 \pm 1.16) \times 10^{15}$
Band 6	HDO (225 GHz)	$(5.98 \pm 0.64) \times 10^{15}$	$(6.00 \pm 0.64) \times 10^{15}$	$(6.84 \pm 0.73) \times 10^{15}$
	HDO (241 GHz)	$(3.36 \pm 0.39) \times 10^{15}$	$(5.92 \pm 0.69) \times 10^{15}$	$(7.31 \pm 0.85) \times 10^{15}$
Band 7	H_2^{16}O (321 GHz) ^a	$\leq 1.16 \times 10^{24}$	$\leq 2.20 \times 10^{18}$	$\leq 3.81 \times 10^{17}$
	H_2^{18}O (322 GHz)	$(2.86 \pm 0.50) \times 10^{16}$	$(2.75 \pm 0.48) \times 10^{15}$	$(2.24 \pm 0.39) \times 10^{15}$
	HDO (335 GHz)	$(5.98 \pm 0.67) \times 10^{15}$	$(1.63 \pm 0.18) \times 10^{15}$	$(1.54 \pm 0.17) \times 10^{15}$

^a3 σ upper limits are estimated for non-detection.

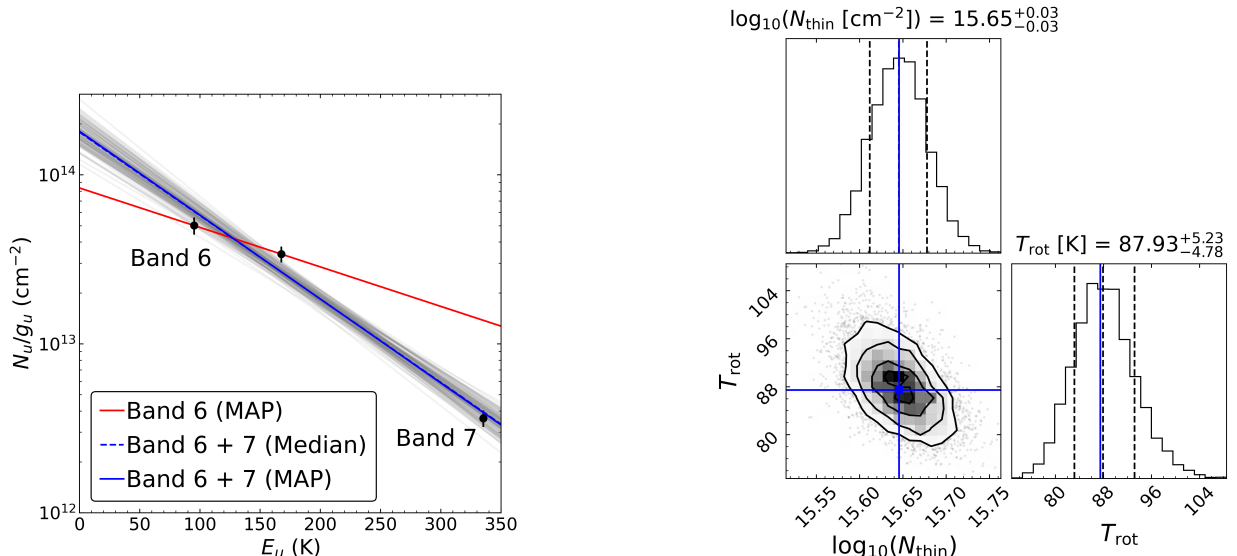


Figure 8. Left: Rotational diagram based on three HDO lines observed with ALMA Bands 6 and 7. The blue dashed line represents the median result from the MCMC sampling, while the blue solid line shows the best-fit model corresponding to the maximum a posteriori (MAP) estimate; the dashed and solid lines almost overlap. Gray solid lines indicate a subset of MCMC samples, illustrating the uncertainty in the fit. For comparison, the red solid line shows the MAP estimate derived from an MCMC analysis using only the two Band 6 HDO lines reported by J. J. Tobin et al. (2023) (see Appendix C for the rotational diagram). Right: Corner plot showing the results of the MCMC sampling for the rotational diagram fitting based on three HDO lines. The black dashed lines indicate the 16th, 50th, and 84th percentiles of the posterior distributions, with the corresponding values shown at the top of each panel, while the blue solid lines represent MAP estimates.

The H_2O total column densities were estimated from the H_2^{18}O column densities listed in Table 5, detected in Bands 5 and 7, by adopting the corresponding isotopic ratio ($^{16}\text{O}/^{18}\text{O} = 560 \pm 25$) (T. L. Wilson & R. Rood 1994). Based on these values, we derived the water vapor abundances with respect to molecular hydrogen, expressed as $N_{\text{H}_2\text{O}}/N_{\text{H}_2}$, for excitation temperatures of $T_{\text{ex}} = 75$, 180, and 225 K. The results are summarized in Table 6. The derived values of water vapor abundance are between 3×10^{-7} – 5×10^{-6} . The variation in the abundance trends between Bands 5 and 7 with differ-

ent assumed excitation temperatures T_{ex} is attributable to the differences in the upper state energies E_u of the H_2^{18}O lines in each band, as discussed in Section 3.5.

If water molecules are mostly inherited from dark clouds and pre-stellar cores, the water abundance should be $\sim 10^{-4}$ (e.g., A. C. A. Boogert et al. 2015). However, recent water line observations toward several Class 0 low-mass protostars suggest low water gas fractional abundances ($\sim 10^{-7}$ – 10^{-6}) in the inner warm envelopes ($r < 10^2$ au, within its water snowline, e.g., M. V. Persson et al. 2012, 2016; E. F. van Dishoeck et al. 2021,

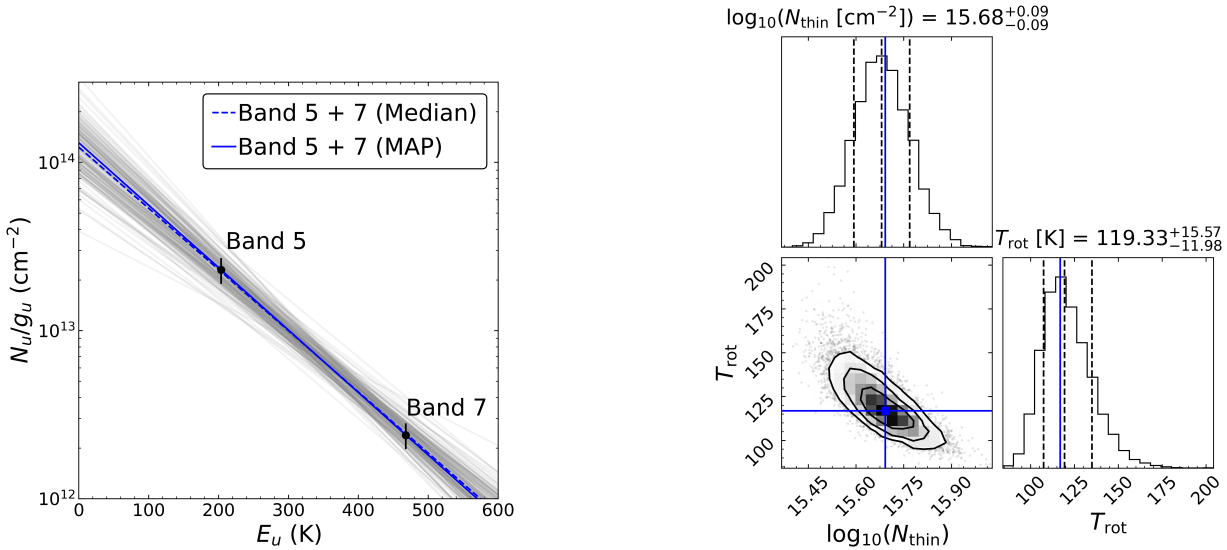


Figure 9. The same as Figure 8, but for two H_2^{18}O lines observed with ALMA Bands 5 and 7.

Table 6. Water abundances at different excitation temperatures T_{ex}

Band	$\log(N_{\text{H}_2\text{O}}/N_{\text{H}_2})$		
	$(T_{\text{ex}} = 75 \text{ K})$	$(T_{\text{ex}} = 180 \text{ K})$	$(T_{\text{ex}} = 225 \text{ K})$
Band 5	-5.93 ± 0.08	-6.06 ± 0.08	-6.02 ± 0.08
Band 7	-5.39 ± 0.08	-6.40 ± 0.08	-6.49 ± 0.08

2025). S. Notsu et al. (2021) suggested that X-ray-induced destruction processes of water (ion-molecule reactions and the X-ray-induced photodissociation) can explain the observed lower water abundances in the inner envelopes of these objects.

In addition, D. Harsono et al. (2020) conducted water line observations with ALMA and NOEMA and showed that water vapor is not abundant in the warm envelopes and disks around Class I protostars, and upper limit values of the water gas abundance averaged over the inner warm disk with $> 100 \text{ K}$ are $\sim 10^{-7}$ – 10^{-5} . These lower water gas abundances might also be caused by efficient water gas destruction through X-ray-induced chemistry, in addition to locking up water in icy dust grains (see also S. Notsu et al. 2021). Our derived values of water vapor abundances for the V883 Ori disk fall within this range, indicating that the water abundances of the V883 Ori disk inferred from our observations are consistent with previous studies of Class I and several Class 0 protostellar envelopes and disks.

4.2. $\text{HDO}/\text{H}_2\text{O}$ ratio

We derived the $\text{HDO}/\text{H}_2\text{O}$ abundance ratios using total column densities calculated from observed line pairs. The H_2^{18}O column densities were converted to H_2^{16}O by applying the isotopic ratio ($^{16}\text{O}/^{18}\text{O} = 560 \pm 25$) (T. L. Wilson & R. Rood 1994), enabling a direct comparison between HDO and the main isotopologue of water. The D/H ratios were calculated using the relation $\text{HDO}/\text{H}_2\text{O} = 2 \times \text{D}/\text{H}$. The analysis was performed assuming excitation temperatures of 75 K, 180 K, and 225 K, following the same assumptions as J. J. Tobin et al. (2023), and the results were summarized for each line pair in Table 7 and Figure 10. Although in our analyses the $\text{HDO}/\text{H}_2\text{O}$ abundance ratios estimated from line pairs observed in Band 7 tend to be lower than those derived from line pairs observed in Bands 5 and 6 (see Table 7 and Figure 10), these results do not contradict the range of ratios reported in previous studies (J. J. Tobin et al. 2023).

The abundance of deuterated species becomes enhanced in the cold ISM due to deuterium becoming locked into H_2D^+ , and the dissociative recombination of deuterated molecules increases the free deuterium available for HDO and D_2O formation within ice mantles of dust grains (K. Furuya et al. 2016, 2017; E. F. van Dishoeck et al. 2021; H. Nomura et al. 2023). In contrast, within the warm gas in the inner envelopes around Class 0 protostars, where ices have sublimated, the ratios have been measured more precisely with ALMA and NOEMA and found to lie roughly between 6×10^{-4} and 2×10^{-3} (e.g., M. V. Persson et al. 2014; S. S. Jensen et al. 2019, 2021; D. Harsono et al. 2020; S. Notsu et al. 2021; J. J. Tobin et al. 2023; E. F. van Dishoeck et al.

2025). Recently, the HDO/H₂O ice ratios in low-mass protostars are reported as $\sim 5 \times 10^{-3}$ from JWST spectra (K. Slavcinska et al. 2025; E. F. van Dishoeck et al. 2025). The HDO/H₂O in comets range between 10^{-4} and 10^{-3} (e.g., K. Altwegg et al. 2015, 2019; H. Nomura et al. 2023; M. A. Cordiner et al. 2025). The HDO/H₂O abundance ratios of the V883 Ori disk reported in our analyses and other studies (J. J. Tobin et al. 2023; M. Leemker et al. 2025b) are comparable to the values reported in Class 0 protostars for water vapor and ice, and also similar to the values for many Oort Cloud comets and 67P/Churyumov-Gerasimenko from the Jupiter Family System (e.g., K. Altwegg et al. 2015, 2019; J. J. Tobin et al. 2023), suggesting that water in the V883 Ori would be directly inherited from the infalling protostellar envelopes (K. Furuya et al. 2016, 2017; E. F. van Dishoeck et al. 2021).

4.3. Band 7 HDO Line Weakness Relative to Rotational Diagram Predictions

Section 3.4 demonstrated that the Band 7 HDO transition at 335 GHz falls well below the trend defined by the Band 6 lines, with an observed intensity roughly a quarter of the expected strength. Here, we examine possible causes for this discrepancy.

4.3.1. Possibility of a more compact emitting region

A comparison of the upper state energies (E_u) of the detected HDO transitions reveals that the Band 6 lines at 225 GHz and 241 GHz (with $E_u = 167$ K and 95 K, respectively) are excited under significantly cooler conditions than the Band 7 transition at 335 GHz ($E_u = 335$ K). This suggests that the 335 GHz line could originate in warmer regions, likely closer to the central protostar.

Under the assumption that line intensity scales approximately with the emitting area, the relatively weak intensity of the 335 GHz transition implies a more compact emission region. Assuming the same inner-disk obscuration assumption used in the Band 6 analysis—i.e., that the inner 40 au is heavily obscured by dust and contributes little to the observed emission—and adopting ~ 80 au as the emission radius for the Band 6 HDO line (J. J. Tobin et al. 2023), we estimate an effective emission radius of about 53 au for the Band 7 HDO line.

This interpretation is consistent with previous theoretical studies (S. Notsu et al. 2016, 2017, 2018), which argue that water lines with relatively low Einstein A coefficients and high excitation energies serve as effective tracers of hot water vapor inside the snowline, where dust temperatures are sufficiently high to enable thermal desorption. Transitions such as para-H₂¹⁸O 5_{1,5}–4_{2,2} at

322 GHz and HDO 3_{3,1}–4_{2,2} at 335 GHz (along with undetected lines like ortho-H₂¹⁶O 10_{2,9}–9_{3,6} at 321 GHz) have been identified as valuable tracers of warm water in the inner disk.

Therefore, our conclusion that the 335 GHz HDO emission arises from a more compact, warmer region than that traced by the Band 6 lines is not only observationally supported, but also theoretically plausible.

4.3.2. Possibility of a larger central depression due to dust optical depth

Dust opacity can significantly attenuate molecular line emission from the innermost regions, as previously demonstrated for this source (M. L. R. van 't Hoff et al. 2018; J.-E. Lee et al. 2019; Y. Yamato et al. 2024). Furthermore, M. De Simone et al. (2020) found that dust absorption at millimeter wavelengths can substantially reduce the intensity of optically thin lines, leading to underestimates of molecular abundances and an apparent deficiency in the detected COMs. In (sub)millimeter observations, bright dust continuum emission can often obscure molecular lines, especially for species residing in the disk midplane. In the case of V883 Ori, the dust optical depth at the disk midplane ($r \sim 42$ au) could exceed $\tau_{\text{dust}} \gtrsim 2$ (L. A. Cieza et al. 2016), potentially causing significant underestimates of molecular line intensities from this region.

J.-H. Jeong et al. (2025) estimated the averaged dust optical depth, $\tau_{\nu, \text{dust}}$, over the COM-emitting region, $\sim 0''.1$ – $0''.3$ (J.-E. Lee et al. 2024), using the following equation:

$$\tau_{\nu, \text{dust}} = (N_{\text{H}_2, \text{cavity}} \cdot \kappa_{\text{ref}} \cdot m_{\text{H}_2} \cdot 0.01) \cdot \left(\frac{\nu}{\nu_{\text{ref}}} \right)^{\beta} \quad (5)$$

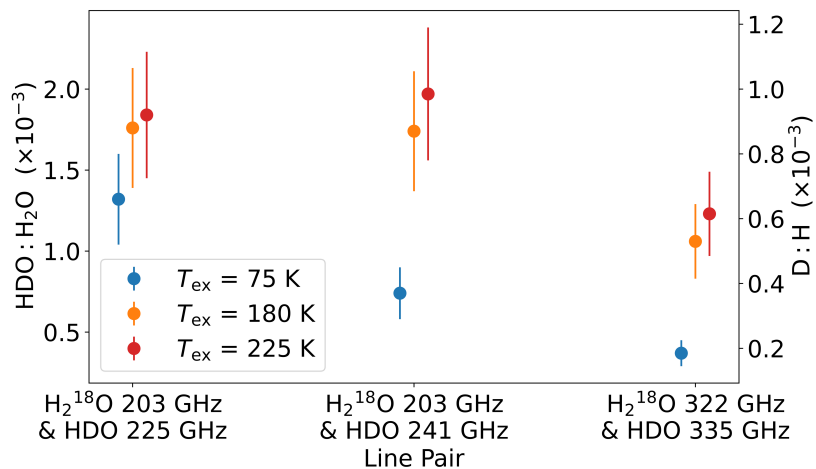
In this study, we adopt the same approach, using observational parameters derived from Band 6 data. We assume a dust mass opacity $\kappa_{\text{ref}} = 2.2 \text{ cm}^2 \text{ g}^{-1}$ at $\nu_{\text{ref}} = 230$ GHz and a dust opacity spectral index $\beta = 1$, following L. A. Cieza et al. (2018). We also adopt the molecular hydrogen column density $N_{\text{H}_2, \text{cavity}} = 1.24 \times 10^{25} \text{ cm}^{-2}$ as derived by J.-H. Jeong et al. (2025).

By substituting these values into Equation (5), we estimate $\tau_{\nu, \text{dust}}$ and the corresponding line attenuation due to dust extinction ($e^{-\tau_{\nu, \text{dust}}}$) for the three isotopologue water lines reported in J. J. Tobin et al. (2023) and the two lines detected in this study. The results are summarized in Table 8.

Based on our calculations, the water lines detected in Band 7 are subject to dust attenuation somewhat stronger than those detected in Bands 5 and 6, by a factor of roughly 1.4–1.6. This qualitatively agrees with our observational result that the Band 7 HDO line in-

Table 7. Derived HDO/H₂O abundance ratios at different excitation temperatures

Line Pair	HDO/H ₂ O		
	($T_{\text{ex}} = 75 \text{ K}$)	($T_{\text{ex}} = 180 \text{ K}$)	($T_{\text{ex}} = 225 \text{ K}$)
H ₂ ¹⁸ O (203 GHz), HDO (225 GHz)	(1.32 ± 0.28) $\times 10^{-3}$	(1.76 ± 0.37) $\times 10^{-3}$	(1.84 ± 0.39) $\times 10^{-3}$
H ₂ ¹⁸ O (203 GHz), HDO (241 GHz)	(0.74 ± 0.16) $\times 10^{-3}$	(1.74 ± 0.37) $\times 10^{-3}$	(1.97 ± 0.41) $\times 10^{-3}$
H ₂ ¹⁸ O (322 GHz), HDO (335 GHz)	(0.37 ± 0.08) $\times 10^{-3}$	(1.06 ± 0.23) $\times 10^{-3}$	(1.23 ± 0.26) $\times 10^{-3}$

**Figure 10.** HDO/H₂O abundance ratios derived from pairs of water isotopologue lines observed in Band 5, 6, and 7 at excitation temperatures of 75, 180, and 225 K. Vertical error bars represent 1 standard deviation uncertainties for each data point.**Table 8.** $\tau_{\nu, \text{dust}}, e^{-\tau_{\nu, \text{dust}}}$

Isotope (Frequency)	$\tau_{\nu, \text{dust}}$	$e^{-\tau_{\nu, \text{dust}}}$
Band 5		
H ₂ ¹⁸ O (203 GHz)	0.80	0.45
Band 6		
HDO (225 GHz)	0.89	0.41
HDO (241 GHz)	0.96	0.39
Band 7		
H ₂ ¹⁸ O (322 GHz)	1.28	0.28
HDO (335 GHz)	1.33	0.27

tensities are weaker than predicted. However, quantitatively, the observed Band 7 HDO lines are only about one-quarter of the predicted values. To quantitatively explain the weaker Band 7 water line compared to the Band 6 lines by the stronger dust attenuation, one potential approach is to attribute it to the difference in sizes of the dust-induced cavity regions in the disk center reported by [J. J. Tobin et al. \(2023\)](#). If the reduced in-

tensity of the HDO line observed in Band 7 is attributed to the frequency-dependent impact of the dust-induced cavity, this implies that the apparent cavity radius is ~ 40 au at Band 6 but increases to ~ 60 au at Band 7. However, the spatial resolution of the observations presented in this study is insufficient to resolve such cavities clearly.

4.3.3. Future Prospects

As discussed above, the significant reduction in the observed Band 7 HDO line intensity compared with the Band 6 HDO line can be interpreted as arising from (i) a more compact emitting region due to the higher upper state energy transition, (ii) an expansion of the apparent cavity caused by dust continuum absorption affecting the line emission, or (iii) a combination of both effects. Considering that the excitation temperature of the Band 7 H₂¹⁸O line is also estimated to be relatively low, its weaker intensity compared with the Band 5 H₂¹⁸O line may similarly be attributed to the same factors affecting the Band 7 HDO line.

However, the spatial resolution of the observations presented in this study is insufficient to directly resolve

the extent of the emitting region or to clearly identify the apparent cavity structure due to dust optical depth, as illustrated in Figure 6 and 7. Therefore, to definitively determine the cause of the significantly lower Band 7 HDO intensity compared to the value predicted from Band 6 observations (e.g., J. J. Tobin et al. 2023), observations with higher spatial resolution will be indispensable.

5. SUMMARY

We observed the protoplanetary disk around the FU Ori-type star V883 Ori with ALMA Band 7 and detected two targeted transitions of water: para- H_2^{18}O $5_{1,5}-4_{2,2}$ at 322 GHz and HDO $3_{3,1}-4_{2,2}$ at 335 GHz. By carefully removing blends with nearby molecular lines, we estimated the intrinsic line fluxes of the detected water transitions. With the correction for Keplerian rotation applied, HDO and H_2^{18}O were detected with significances of 23.6σ and 9.3σ , respectively. Combining these Band 7 detections with previously reported water lines in Band 5 and 6, we constructed rotational diagrams to derive the column densities and rotational temperatures of each water isotopologue. From the derived column densities, we estimated water vapor abundances relative to H_2 at the water snowline (~ 80 au), obtaining values of 3×10^{-7} – 5×10^{-6} . Note that our derived water abundance value is the averaged value in the vertical direction. These abundances are consistent with the low water gas fractions reported for Class 0 and I protostellar envelopes and disks, which may be explained by X-ray induced destruction and/or water locked in icy grains. We also derived HDO/ H_2O abundance ratios in the range $(0.4\text{--}2.0) \times 10^{-3}$, comparable to values measured in gas and ice in Class 0 protostellar envelopes and comets, suggesting that water in the V883 Ori disk is largely inherited from the parental protostellar envelope.

We found that the Band 7 HDO lines are significantly weaker than expected based on the rotational diagram derived from the Band 6 transitions. This discrepancy suggests that the Band 7 emission could arise from a more compact and narrow region than the Band 6 lines. Such a compact emitting region may result from the higher upper state energies of the Band 7 lines, which trace hotter gas located closer to the central protostar, and/or from higher optical depths, which would make the central dust cavity appear larger than in the Band 6 observations due to stronger dust absorption. Taken together, our analysis indicates that the V883 Ori disk shows water abundances and isotopic ratios consistent

with inheritance from protostellar envelopes, while the weakness of the Band 7 HDO lines points to more compact or optically thick emission. To distinguish between these possibilities and to constrain the precise spatial distribution of the Band 7 water emission, higher angular resolution follow-up observations are needed.

ACKNOWLEDGMENTS

The authors thank the anonymous referee for comments. We are grateful to Professor J. J. Tobin for valuable suggestions on the analysis code and to Dr. Nanase Harada for useful comments. We are also grateful to the summer student program at the National Astronomical Observatory of Japan / Astronomical Science Program of SOKENDAI, where this research initially took place. This paper makes use of the following ALMA data: ADSJAO.ALMA#2021.1.00115.S and #2021.1.00186.S. ALMA is a partnership of ESO (representing its member states), NSF (USA), and NINS (Japan), together with NRC (Canada), MOST, ASIAA (Taiwan), and KASI (Republic of Korea), in cooperation with the Republic of Chile. The Joint ALMA Observatory is operated by ESO, AUI/NRAO, and NAOJ. ALMA Data analysis was carried out on the Multi-wavelength Data Analysis System operated by the Astronomy Data Center (ADC), National Astronomical Observatory of Japan. H.N was supported by the ALMA Japan Research Grant of NAOJ ALMA Project, NAOJ-ALMA-374. S.N. is grateful for support from Grants-in-Aid for JSPS (Japan Society for the Promotion of Science) Fellows grant No. JP23KJ0329, MEXT/JSPS Grants-in-Aid for Scientific Research (KAKENHI) grant Nos. JP23K13155, JP24K00674, and JP23H05441, and Start-up Research Grant as one of The University of Tokyo Excellent Young Researcher 2024. T.H. is financially supported by the MEXT/JSPS KAKENHI grant Nos. 17K05398, 18H05222, and 20H05845. T.C.Y. thanks for support from Grants-in-Aid for JSPS Fellows grant No. JP23KJ1008.

Facility: ALMA

Software: CASA (CASA Team et al. 2022), Astropy (Astropy Collaboration et al. 2013, 2018, 2022), GoFish (R. Teague 2019), Numpy (C. R. Harris et al. 2020), Scipy (P. Virtanen et al. 2020), Matplotlib (J. D. Hunter 2007), Emcee (D. Foreman-Mackey et al. 2013), corner.py (D. Foreman-Mackey 2016)

APPENDIX

A. DISK-INTEGRATED SPECTRA

Figure 11 displays the disk-integrated spectrum for each spectral window. The observed line profiles exhibit characteristic double-peaked shapes, indicative of Keplerian rotation. To recover the intrinsic line shapes, we applied spectral alignment using `GoFish`, which effectively removes the velocity gradients introduced by rotation. The aligned spectra (Figure 12) exhibit single-peaked profiles centered around the systemic velocity. Short black lines above the spectra indicate the frequencies of detected contaminated lines. The corresponding rest frequencies are summarized in Table 3, and these values were used to create the Keplerian masks shown in Figures 4 and 5. The expected positions of the targeted water lines at the systemic velocity are marked with blue dashed lines.

B. COMPARISON OF MODEL SPECTRA FOR FITTING

The spectral fitting was performed using template spectra constructed from molecular lines detected in the observational data. Specifically, we employed two types of template spectra: one based on the CH₃OH 242 GHz lines detected in Band 6, as used in [J. J. Tobin et al. \(2023\)](#) (the Band 6 template), and the other based on the CH₃CHO 335 GHz line detected in our Band 7 data (the Band 7 template).

Using both templates, we fitted the spectra to derive the integrated intensities (see Figure 13) and their uncertainties for the water isotopologue lines. The uncertainties were estimated from the residuals in the frequency range corresponding to each target line.

For all water isotopologue lines in Bands 5, 6, and 7, the uncertainties were systematically smaller when using the Band 7-based template (see Table 9). This difference may arise from the fact that the lines used to construct the Band 6 template could be optically thick, resulting in a different line profile. Therefore, we adopted the fitting results from the Band 7 template for the subsequent calculations of column densities and excitation temperatures.

We also compared the line profiles of the HDO lines detected in Band 5 and 6 by [J. J. Tobin et al. \(2023\)](#) with those of the Band 7 HDO line detected in this work, in addition to the model profiles. As a result, we did not find any significant difference in the peak positions of the lines. The line profiles correspond to the emitting regions of each transition ([S. Notsu et al. 2016, 2017,](#)

2018). Assuming the emitting region of 53 au estimated in Section 4.3.1, the difference between this size and the emitting region of 80 au inferred from the Band 7 observations corresponds to only a factor of 1.5 in radius, or

Table 9. Integrated intensities derived from fitting using Band 6 and Band 7 template spectra I_{int}

Line	$I_{\text{int, Band 6}}$ (mJy km s ⁻¹)	$I_{\text{int, Band 7}}$ (mJy km s ⁻¹)
Band 5		
H ₂ ¹⁸ O (203 GHz)	168.51 ± 23.78	144.52 ± 20.75
Band 6		
HDO (225 GHz)	588.70 ± 24.37	585.92 ± 22.14
HDO (241 GHz)	528.00 ± 35.32	555.59 ± 32.82
Band 7		
H ₂ ¹⁶ O (321 GHz)	-	-
H ₂ ¹⁸ O (322 GHz)	55.96 ± 8.01	52.06 ± 7.48
HDO (335 GHz)	133.00 ± 9.37	123.73 ± 6.15

NOTE— $I_{\text{int, Band 6}}$ and $I_{\text{int, Band 7}}$ were derived by fitting template spectra constructed from detected contaminated lines in Band 6 and Band 7, respectively. For H₂¹⁶O (321 GHz), the line was not detected. The 3σ upper limit is listed in Table 4.

a factor of 1.2 in the corresponding Keplerian velocity. Therefore, given the spectral resolution of each observation, the lack of a clear difference in the peak positions for this low-mass object is hardly avoidable.

C. ROTATIONAL DIAGRAM OF HDO IN ALMA BAND 6

Figure 14 shows the rotational diagram constructed from the two Band 6 HDO lines reported by [J. J. Tobin et al. \(2023\)](#). The red solid line in the figure represents the MAP estimate from our MCMC analysis, which corresponds to the red solid line shown in Figure 8. The results of the MAP estimation indicate that HDO has a rotational temperature of 186.4 K and a logarithmic column density of $\log(N[\text{cm}^{-2}]) = 15.79$. As noted in Section 3.2, our treatment of the HDO line intensities differs from that of [J. J. Tobin et al. \(2023\)](#) in that we use the integrated fluxes of the fitted spectral models rather than direct flux measurements. Nevertheless, the derived column densities and rotational temperatures are consistent within the 1σ uncertainties.

REFERENCES

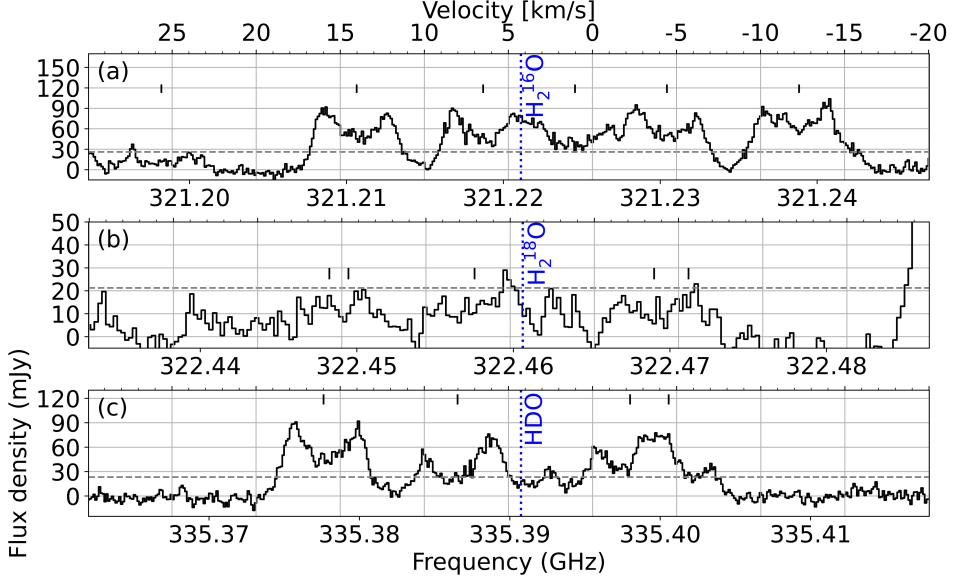


Figure 11. Disk-integrated spectra for the three spectral windows targeting the H_2^{16}O 321 GHz, H_2^{18}O 322 GHz, and HDO 335 GHz lines (from top to bottom). The spectra exhibit double-peaked profiles due to Keplerian rotation. Short black lines above the spectra indicate the frequencies of detected contaminated lines.

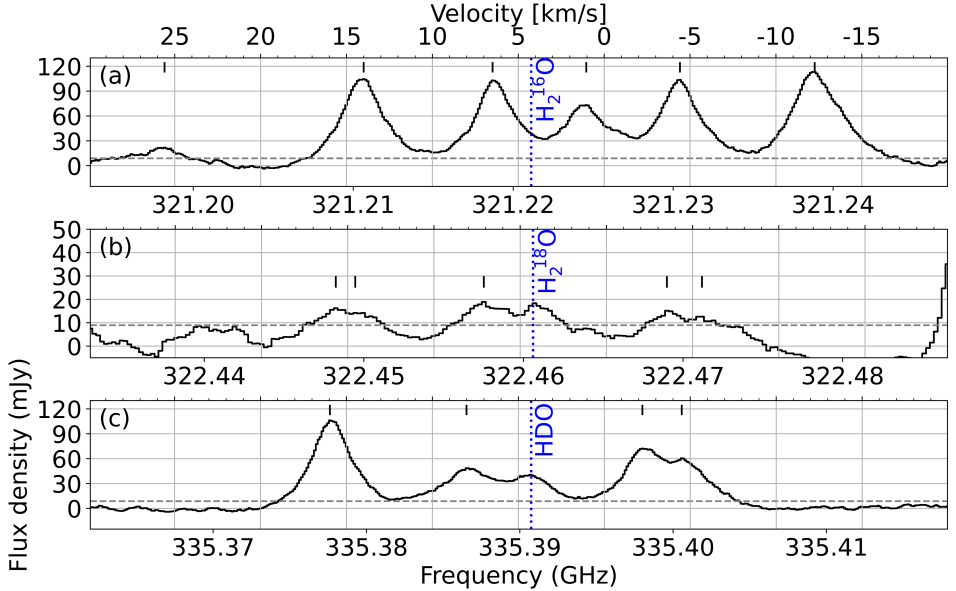


Figure 12. Velocity-aligned spectra of the same lines as in Figure 11, obtained using `GoFish`. The alignment removes rotational broadening and yields single-peaked profiles. Short black lines above the spectra mark the rest frequencies of detected contaminated lines.

Altwegg, K., Balsiger, H., & Fuselier, S. A. 2019, *ARA&A*,

57, 113, doi: [10.1146/annurev-astro-091918-104409](https://doi.org/10.1146/annurev-astro-091918-104409)

Altwegg, K., Balsiger, H., Bar-Nun, A., et al. 2015, *Science*, 347, 1261952, doi: [10.1126/science.1261952](https://doi.org/10.1126/science.1261952)

Astropy Collaboration, Robitaille, T. P., Tollerud, E. J., et al. 2013, *Astronomy and Astrophysics*, 558, A33, doi: [10.1051/0004-6361/201322068](https://doi.org/10.1051/0004-6361/201322068)

Astropy Collaboration, Price-Whelan, A. M., Sipőcz, B. M., et al. 2018, *The Astronomical Journal*, 156, 123,

doi: [10.3847/1538-3881/aabc4f](https://doi.org/10.3847/1538-3881/aabc4f)

Astropy Collaboration, Price-Whelan, A. M., Lim, P. L., et al. 2022, *The Astrophysical Journal*, 935, 167, doi: [10.3847/1538-4357/ac7c74](https://doi.org/10.3847/1538-4357/ac7c74)

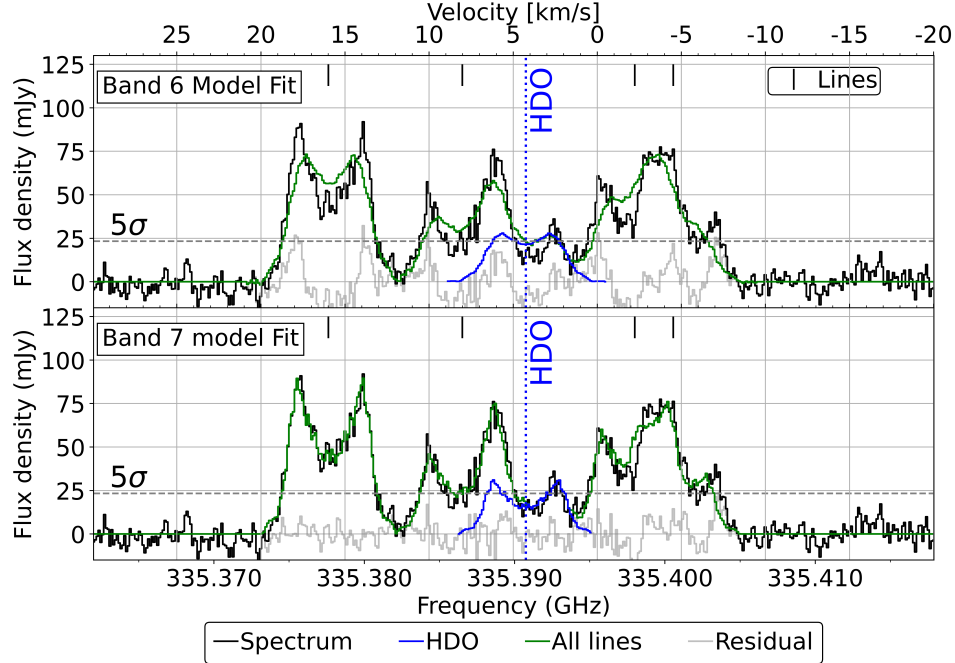


Figure 13. Spectra around the HDO 335 GHz emission line observed in Band 7, with fitting results based on model spectra derived from Band 6 (upper panels) and Band 7 (lower panels) data. The black solid lines represent the observed spectra. The blue dotted line indicates the frequency of the HDO line corresponding to the systemic velocity of V883 Ori (4.25 km s^{-1}), while the blue solid lines show the fitted models for the HDO line. The green solid lines represent the combined fitting models including the HDO line and contaminated lines. The gray solid lines represent the residuals obtained by subtracting the model spectrum from the observed data. Vertical black ticks indicate the central frequencies of the contaminated lines, and the gray dashed lines correspond to the 5σ noise level. The fitting using the template derived from Band 7 spectrum achieves a more accurate reproduction of the observed features compared to that using the Band 6 template.

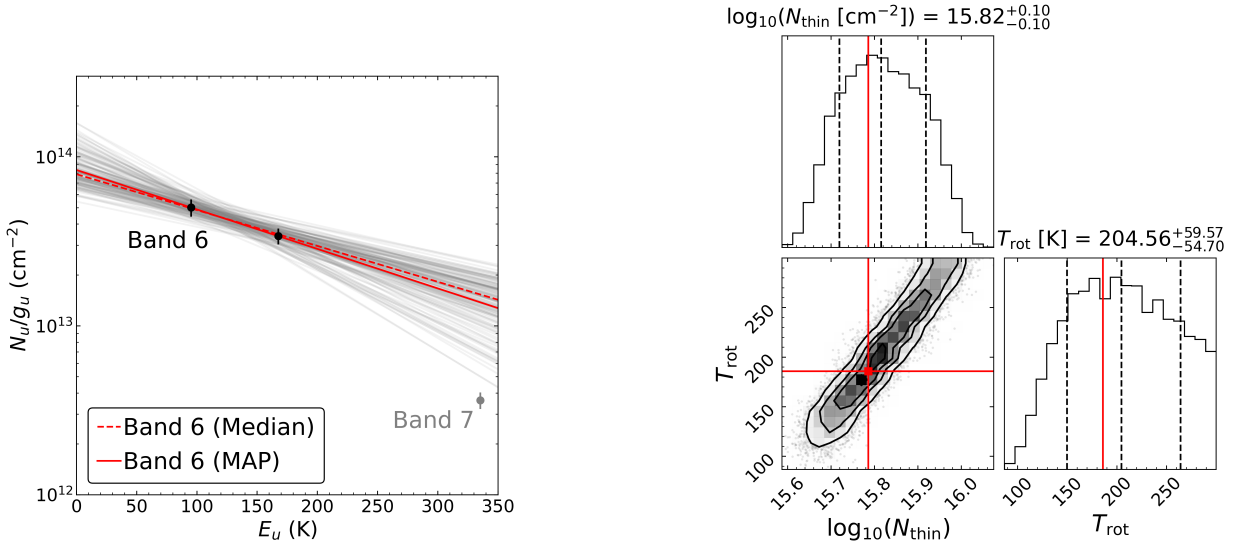


Figure 14. The same as Figure 8, but for two HDO lines observed with ALMA Band 6.

Banzatti, A., Pinilla, P., Ricci, L., et al. 2015, The Astrophysical Journal, 815, L15, doi: [10.1088/2041-8205/815/1/L15](https://doi.org/10.1088/2041-8205/815/1/L15)

Banzatti, A., Pontoppidan, K. M., Carr, J. S., et al. 2023, ApJL, 957, L22, doi: [10.3847/2041-8213/acf5ec](https://doi.org/10.3847/2041-8213/acf5ec)
 Bjerke, P., Jørgensen, J. K., Bergin, E. A., et al. 2016, A&A, 595, A39, doi: [10.1051/0004-6361/201628795](https://doi.org/10.1051/0004-6361/201628795)

Boogert, A. C. A., Gerakines, P. A., & Whittet, D. C. B. 2015, *ARA&A*, 53, 541, doi: [10.1146/annurev-astro-082214-122348](https://doi.org/10.1146/annurev-astro-082214-122348)

Bosman, A. D., & Bergin, E. A. 2021, *ApJL*, 918, L10, doi: [10.3847/2041-8213/ac1db1](https://doi.org/10.3847/2041-8213/ac1db1)

Calahan, J. K., Bergin, E. A., van't Hoff, M., et al. 2024, *ApJ*, 975, 170, doi: [10.3847/1538-4357/ad78d1](https://doi.org/10.3847/1538-4357/ad78d1)

CASA Team, Bean, B., Bhatnagar, S., et al. 2022, *Publications of the Astronomical Society of the Pacific*, 134, 114501, doi: [10.1088/1538-3873/ac9642](https://doi.org/10.1088/1538-3873/ac9642)

Ceccarelli, C., Codella, C., Balucani, N., et al. 2023, in *Protostars and Planets VII*, Vol. 534, 379

Cieza, L. A., Casassus, S., Tobin, J., et al. 2016, *Nature*, 535, 258, doi: [10.1038/nature18612](https://doi.org/10.1038/nature18612)

Cieza, L. A., Ruíz-Rodríguez, D., Perez, S., et al. 2018, *Monthly Notices of the Royal Astronomical Society*, 474, 4347, doi: [10.1093/mnras/stx3059](https://doi.org/10.1093/mnras/stx3059)

Cordiner, M. A., Gibb, E. L., Kisiel, Z., et al. 2025, *Nature Astronomy*, doi: [10.1038/s41550-025-02614-7](https://doi.org/10.1038/s41550-025-02614-7)

De Simone, M., Ceccarelli, C., Codella, C., et al. 2020, *The Astrophysical Journal*, 896, L3, doi: [10.3847/2041-8213/ab8d41](https://doi.org/10.3847/2041-8213/ab8d41)

Facchini, S., Testi, L., Humphreys, E., et al. 2024, *Nature Astronomy*, 8, 587, doi: [10.1038/s41550-024-02207-w](https://doi.org/10.1038/s41550-024-02207-w)

Fadul, A. M. A., Schwarz, K. R., Suhasaria, T., et al. 2025a, *ApJL*, 988, L44, doi: [10.3847/2041-8213/adec6e](https://doi.org/10.3847/2041-8213/adec6e)

Fadul, A. M. A., Schwarz, K. R., van't Hoff, M. L. R., et al. 2025b, *AJ*, 169, 307, doi: [10.3847/1538-3881/adc998](https://doi.org/10.3847/1538-3881/adc998)

Foreman-Mackey, D. 2016, *Journal of Open Source Software*, 1, 24, doi: [10.21105/joss.00024](https://doi.org/10.21105/joss.00024)

Foreman-Mackey, D., Hogg, D. W., Lang, D., & Goodman, J. 2013, *Publications of the Astronomical Society of the Pacific*, 125, 306, doi: [10.1086/670067](https://doi.org/10.1086/670067)

Furlan, E., Fischer, W. J., Ali, B., et al. 2016, *The Astrophysical Journal Supplement Series*, 224, 5, doi: [10.3847/0067-0049/224/1/5](https://doi.org/10.3847/0067-0049/224/1/5)

Furuya, K., Drozdovskaya, M. N., Visser, R., et al. 2017, *A&A*, 599, A40, doi: [10.1051/0004-6361/201629269](https://doi.org/10.1051/0004-6361/201629269)

Furuya, K., van Dishoeck, E. F., & Aikawa, Y. 2016, *A&A*, 586, A127, doi: [10.1051/0004-6361/201527579](https://doi.org/10.1051/0004-6361/201527579)

Greene, T. P., Aspin, C., & Reipurth, B. 2008, *The Astronomical Journal*, 135, 1421, doi: [10.1088/0004-6256/135/4/1421](https://doi.org/10.1088/0004-6256/135/4/1421)

Harris, C. R., Millman, K. J., van der Walt, S. J., et al. 2020, *Nature*, 585, 357, doi: [10.1038/s41586-020-2649-2](https://doi.org/10.1038/s41586-020-2649-2)

Harsono, D., Bruderer, S., & van Dishoeck, E. F. 2015, *A&A*, 582, A41, doi: [10.1051/0004-6361/201525966](https://doi.org/10.1051/0004-6361/201525966)

Harsono, D., Persson, M. V., Ramos, A., et al. 2020, *Astronomy & Astrophysics*, 636, A26, doi: [10.1051/0004-6361/201935994](https://doi.org/10.1051/0004-6361/201935994)

Hartmann, L., Calvet, N., Gullbring, E., & D'Alessio, P. 1998, *The Astrophysical Journal*, 495, 385, doi: [10.1086/305277](https://doi.org/10.1086/305277)

Hayashi, C. 1981, *Progress of Theoretical Physics Supplement*, 70, 35, doi: [10.1143/PTPS.70.35](https://doi.org/10.1143/PTPS.70.35)

Hayashi, C., Nakazawa, K., & Nakagawa, Y. 1985, in *Protostars and Planets II*, 1100–1153

Hirota, T., Tsuboi, M., Kurono, Y., et al. 2014, *Publications of the Astronomical Society of Japan*, 66, 106, doi: [10.1093/pasj/psu110](https://doi.org/10.1093/pasj/psu110)

Houge, A., Macías, E., & Krijt, S. 2024, *Monthly Notices of the Royal Astronomical Society*, 527, 9668, doi: [10.1093/mnras/stad3758](https://doi.org/10.1093/mnras/stad3758)

Hunter, J. D. 2007, *Computing in Science & Engineering*, 9, 90, doi: [10.1109/MCSE.2007.55](https://doi.org/10.1109/MCSE.2007.55)

Ida, S., & Guillot, T. 2016, *Astronomy & Astrophysics*, 596, L3, doi: [10.1051/0004-6361/201629680](https://doi.org/10.1051/0004-6361/201629680)

Ida, S., Yamamura, T., & Okuzumi, S. 2019, *A&A*, 624, A28, doi: [10.1051/0004-6361/201834556](https://doi.org/10.1051/0004-6361/201834556)

Jensen, S. S., Jørgensen, J. K., Kristensen, L. E., et al. 2021, *Astronomy & Astrophysics*, 650, A172, doi: [10.1051/0004-6361/202140560](https://doi.org/10.1051/0004-6361/202140560)

Jensen, S. S., Jørgensen, J. K., Kristensen, L. E., et al. 2019, *Astronomy & Astrophysics*, 631, A25, doi: [10.1051/0004-6361/201936012](https://doi.org/10.1051/0004-6361/201936012)

Jeong, J.-H., Lee, J.-E., Lee, S., et al. 2025, *The Astrophysical Journal Supplement Series*, 276, 49, doi: [10.3847/1538-4365/ad9450](https://doi.org/10.3847/1538-4365/ad9450)

Kauffmann, J., Bertoldi, F., Bourke, T. L., Evans, II, N. J., & Lee, C. W. 2008, *Astronomy and Astrophysics*, 487, 993, doi: [10.1051/0004-6361:200809481](https://doi.org/10.1051/0004-6361:200809481)

Kondo, K., Okuzumi, S., & Mori, S. 2023, *ApJ*, 949, 119, doi: [10.3847/1538-4357/acc840](https://doi.org/10.3847/1538-4357/acc840)

Kounkel, M., Covey, K., Suárez, G., et al. 2018, *AJ*, 156, 84, doi: [10.3847/1538-3881/aad1f1](https://doi.org/10.3847/1538-3881/aad1f1)

Lee, J.-E., Lee, S., Baek, G., et al. 2019, *Nature Astronomy*, 3, 314, doi: [10.1038/s41550-018-0680-0](https://doi.org/10.1038/s41550-018-0680-0)

Lee, J.-E., Kim, C.-H., Lee, S., et al. 2024, *The Astrophysical Journal*, 966, 119, doi: [10.3847/1538-4357/ad3106](https://doi.org/10.3847/1538-4357/ad3106)

Leemker, M., Facchini, S., Curone, P., et al. 2025a, *arXiv*, doi: [10.48550/arXiv.2511.16737](https://doi.org/10.48550/arXiv.2511.16737)

Leemker, M., Tobin, J. J., Facchini, S., et al. 2025b, *Nature Astronomy*, 9, 1486, doi: [10.1038/s41550-025-02663-y](https://doi.org/10.1038/s41550-025-02663-y)

Leemker, M., van 't Hoff, M. L. R., Trapman, L., et al. 2021, *Astronomy & Astrophysics*, 646, A3, doi: [10.1051/0004-6361/202039387](https://doi.org/10.1051/0004-6361/202039387)

Lichtenberg, T., Drążkowska, J., Schönbächler, M., Golabek, G. J., & Hands, T. O. 2021, *Science*, 371, 365, doi: [10.1126/science.abb3091](https://doi.org/10.1126/science.abb3091)

Lynden-Bell, D., & Pringle, J. E. 1974, Monthly Notices of the Royal Astronomical Society, 168, 603, doi: [10.1093/mnras/168.3.603](https://doi.org/10.1093/mnras/168.3.603)

Miley, J. M., Panić, O., Booth, R. A., et al. 2021, MNRAS, 500, 4658, doi: [10.1093/mnras/staa3517](https://doi.org/10.1093/mnras/staa3517)

Morbidelli, A., Chambers, J., Lunine, J. I., et al. 2000, Meteoritics & Planetary Science, 35, 1309, doi: [10.1111/j.1945-5100.2000.tb01518.x](https://doi.org/10.1111/j.1945-5100.2000.tb01518.x)

Morbidelli, A., Lunine, J. I., O'Brien, D. P., Raymond, S. N., & Walsh, K. J. 2012, Annual Review of Earth and Planetary Sciences, 40, 251, doi: [10.1146/annurev-earth-042711-105319](https://doi.org/10.1146/annurev-earth-042711-105319)

Morbidelli, A., Bitsch, B., Crida, A., et al. 2016, Icarus, 267, 368, doi: [10.1016/j.icarus.2015.11.027](https://doi.org/10.1016/j.icarus.2015.11.027)

Mori, S., Okuzumi, S., Kunitomo, M., & Bai, X.-N. 2021, ApJ, 916, 72, doi: [10.3847/1538-4357/ac06a9](https://doi.org/10.3847/1538-4357/ac06a9)

Murillo, N. M., Hsieh, T. H., & Walsh, C. 2022, A&A, 665, A68, doi: [10.1051/0004-6361/202142982](https://doi.org/10.1051/0004-6361/202142982)

Nomura, H., Aikawa, Y., Nakagawa, Y., & Millar, T. J. 2009, Astronomy and Astrophysics, 495, 183, doi: [10.1051/0004-6361:200810206](https://doi.org/10.1051/0004-6361:200810206)

Nomura, H., Furuya, K., Cordiner, M. A., et al. 2023, in Astronomical Society of the Pacific Conference Series, Vol. 534, Protostars and Planets VII, ed. S. Inutsuka, Y. Aikawa, T. Muto, K. Tomida, & M. Tamura, 1075

Notsu, S., Nomura, H., Ishimoto, D., et al. 2016, The Astrophysical Journal, 827, 113, doi: [10.3847/0004-637X/827/2/113](https://doi.org/10.3847/0004-637X/827/2/113)

Notsu, S., Nomura, H., Ishimoto, D., et al. 2017, The Astrophysical Journal, 836, 118, doi: [10.3847/1538-4357/836/1/118](https://doi.org/10.3847/1538-4357/836/1/118)

Notsu, S., Nomura, H., Walsh, C., et al. 2018, The Astrophysical Journal, 855, 62, doi: [10.3847/1538-4357/aaaa72](https://doi.org/10.3847/1538-4357/aaaa72)

Notsu, S., Ohno, K., Ueda, T., et al. 2022, ApJ, 936, 188, doi: [10.3847/1538-4357/ac87fa](https://doi.org/10.3847/1538-4357/ac87fa)

Notsu, S., Van Dishoeck, E. F., Walsh, C., Bosman, A. D., & Nomura, H. 2021, Astronomy & Astrophysics, 650, A180, doi: [10.1051/0004-6361/202140667](https://doi.org/10.1051/0004-6361/202140667)

Notsu, S., Akiyama, E., Booth, A., et al. 2019, The Astrophysical Journal, 875, 96, doi: [10.3847/1538-4357/ab0ae9](https://doi.org/10.3847/1538-4357/ab0ae9)

Öberg, K. I., Murray-Clay, R., & Bergin, E. A. 2011, The Astrophysical Journal, 743, L16, doi: [10.1088/2041-8205/743/1/L16](https://doi.org/10.1088/2041-8205/743/1/L16)

Oká, A., Nakamoto, T., & Ida, S. 2011, The Astrophysical Journal, 738, 141, doi: [10.1088/0004-637X/738/2/141](https://doi.org/10.1088/0004-637X/738/2/141)

Okuzumi, S., Tanaka, H., Kobayashi, H., & Wada, K. 2012, The Astrophysical Journal, 752, 106, doi: [10.1088/0004-637X/752/2/106](https://doi.org/10.1088/0004-637X/752/2/106)

Okuzumi, S., & Tazaki, R. 2019, ApJ, 878, 132, doi: [10.3847/1538-4357/ab204d](https://doi.org/10.3847/1538-4357/ab204d)

Persson, M. V., Harsono, D., Tobin, J. J., et al. 2016, A&A, 590, A33, doi: [10.1051/0004-6361/201527666](https://doi.org/10.1051/0004-6361/201527666)

Persson, M. V., Jørgensen, J. K., & van Dishoeck, E. F. 2012, A&A, 541, A39, doi: [10.1051/0004-6361/201117917](https://doi.org/10.1051/0004-6361/201117917)

Persson, M. V., Jørgensen, J. K., van Dishoeck, E. F., & Harsono, D. 2014, Astronomy & Astrophysics, 563, A74, doi: [10.1051/0004-6361/201322845](https://doi.org/10.1051/0004-6361/201322845)

Pickett, H. M., Poynter, R. L., Cohen, E. A., et al. 1998, Journal of Quantitative Spectroscopy and Radiative Transfer, 60, 883, doi: [10.1016/S0022-4073\(98\)00091-0](https://doi.org/10.1016/S0022-4073(98)00091-0)

Pinilla, P., Pohl, A., Stamm, S. M., & Birnstiel, T. 2017, The Astrophysical Journal, 845, 68, doi: [10.3847/1538-4357/aa7edb](https://doi.org/10.3847/1538-4357/aa7edb)

Piso, A.-M. A., Öberg, K. I., Birnstiel, T., & Murray-Clay, R. A. 2015, The Astrophysical Journal, 815, 109, doi: [10.1088/0004-637X/815/2/109](https://doi.org/10.1088/0004-637X/815/2/109)

Piso, A.-M. A., Pegues, J., & Öberg, K. I. 2016, The Astrophysical Journal, 833, 203, doi: [10.3847/1538-4357/833/2/203](https://doi.org/10.3847/1538-4357/833/2/203)

Raymond, S. N., & Izidoro, A. 2017, Icarus, 297, 134, doi: [10.1016/j.icarus.2017.06.030](https://doi.org/10.1016/j.icarus.2017.06.030)

Ros, K., & Johansen, A. 2013, Astronomy and Astrophysics, 552, A137, doi: [10.1051/0004-6361/201220536](https://doi.org/10.1051/0004-6361/201220536)

Ruiz-Rodríguez, D. A., Williams, J. P., Kastner, J. H., et al. 2022, Monthly Notices of the Royal Astronomical Society, 515, 2646, doi: [10.1093/mnras/stac1879](https://doi.org/10.1093/mnras/stac1879)

Sato, T., Okuzumi, S., & Ida, S. 2016, Astronomy & Astrophysics, 589, A15, doi: [10.1051/0004-6361/201527069](https://doi.org/10.1051/0004-6361/201527069)

Schoonenberg, D., & Ormel, C. W. 2017, Astronomy and Astrophysics, 602, A21, doi: [10.1051/0004-6361/201630013](https://doi.org/10.1051/0004-6361/201630013)

Slavínska, K., Tychoniec, Ł., Navarro, M. G., et al. 2025, ApJL, 986, L19, doi: [10.3847/2041-8213/addb45](https://doi.org/10.3847/2041-8213/addb45)

Teague, R. 2019, The Journal of Open Source Software, 4, 1632, doi: [10.21105/joss.01632](https://doi.org/10.21105/joss.01632)

Teague, R. 2020, Zenodo doi: [10.5281/zenodo.4321137](https://doi.org/10.5281/zenodo.4321137)

Tobin, J. J., Van 'T Hoff, M. L. R., Leemker, M., et al. 2023, Nature, 615, 227, doi: [10.1038/s41586-022-05676-z](https://doi.org/10.1038/s41586-022-05676-z)

van Dishoeck, E. F., Kristensen, L. E., Mottram, J. C., et al. 2021, A&A, 648, A24, doi: [10.1051/0004-6361/202039084](https://doi.org/10.1051/0004-6361/202039084)

van Dishoeck, E. F., Tychoniec, Ł., Rocha, W. R. M., et al. 2025, A&A, 699, A361, doi: [10.1051/0004-6361/202554444](https://doi.org/10.1051/0004-6361/202554444)

van 't Hoff, M. L. R., Tobin, J. J., Trapman, L., et al. 2018, The Astrophysical Journal Letters, 864, L23, doi: [10.3847/2041-8213/aadb8a](https://doi.org/10.3847/2041-8213/aadb8a)

Virtanen, P., Gommers, R., Oliphant, T. E., et al. 2020, Nature Methods, 17, 261, doi: [10.1038/s41592-019-0686-2](https://doi.org/10.1038/s41592-019-0686-2)

Walsh, K. J., Morbidelli, A., Raymond, S. N., O'Brien, D. P., & Mandell, A. M. 2011, Nature, 475, 206, doi: [10.1038/nature10201](https://doi.org/10.1038/nature10201)

Wilson, T. L., & Rood, R. 1994, Annual Review of Astronomy and Astrophysics, 32, 191, doi: [10.1146/annurev.aa.32.090194.001203](https://doi.org/10.1146/annurev.aa.32.090194.001203)

Yamato, Y., Notsu, S., Aikawa, Y., et al. 2024, The Astronomical Journal, 167, 66, doi: [10.3847/1538-3881/ad11d9](https://doi.org/10.3847/1538-3881/ad11d9)

Zeng, S., Jeong, J.-H., Oyama, T., et al. 2025, AJ, 170, 33, doi: [10.3847/1538-3881/add733](https://doi.org/10.3847/1538-3881/add733)